



**HAL**  
open science

# Resolution enhancement of SMOS brightness temperatures: application to melt detection on the Antarctic and Greenland ice sheets

Pierre Zeiger, Ghislain Picard, Philippe Richaume, Arnaud Mialon, Nemesio Rodriguez-Fernandez

## ► To cite this version:

Pierre Zeiger, Ghislain Picard, Philippe Richaume, Arnaud Mialon, Nemesio Rodriguez-Fernandez. Resolution enhancement of SMOS brightness temperatures: application to melt detection on the Antarctic and Greenland ice sheets. 2024. hal-04623759

**HAL Id: hal-04623759**

**<https://cnrs.hal.science/hal-04623759v1>**

Preprint submitted on 25 Jun 2024

**HAL** is a multi-disciplinary open access archive for the deposit and dissemination of scientific research documents, whether they are published or not. The documents may come from teaching and research institutions in France or abroad, or from public or private research centers.

L'archive ouverte pluridisciplinaire **HAL**, est destinée au dépôt et à la diffusion de documents scientifiques de niveau recherche, publiés ou non, émanant des établissements d'enseignement et de recherche français ou étrangers, des laboratoires publics ou privés.



Distributed under a Creative Commons Attribution - NonCommercial - NoDerivatives 4.0 International License

# Resolution enhancement of SMOS brightness temperatures: application to melt detection on the Antarctic and Greenland ice sheets

Pierre Zeiger<sup>a,\*</sup>, Ghislain Picard<sup>a</sup>, Philippe Richaume<sup>b</sup>, Arnaud Mialon<sup>b</sup>, Nemesio Rodriguez-Fernandez<sup>b</sup>

<sup>a</sup>*Institut des Géosciences de l'Environnement (IGE), CNRS/UGA, Grenoble, France*

<sup>b</sup>*Centre d'Etudes Spatiales de la Biosphère (CESBIO), CNES, Toulouse, France*

---

## Abstract

A large part of the surface of the Greenland Ice Sheet (GrIS) and the margins of Antarctica are melting every summer, affecting their surface mass balance. Wet/dry snow status has been detected for decades using the peaks of brightness temperature at 19 GHz, and more recently at L-band (1.4 GHz) using both the SMOS and SMAP missions. SMOS owns a longer time series than SMAP with data since 2010, but the 52.5° incidence bin in the Level 3 (L3) product from Centre Aval de Traitement des Données SMOS (CATDS) that was previously used to detect melt suffers from a coarse spatial resolution. For this reason, we developed a new SMOS enhanced resolution brightness temperature ( $T_B$ ) product building on the radiometer version of the Scatterometer Image Reconstruction (rSIR) algorithm. We also exploited the SMOS L1C observations near 40° incidence angle instead of 52.5° as the native spatial resolution of SMOS is better at low incidence. The new product is posted on a 12.5 km polar stereographic grid and covers all the GrIS and Antarctica for 2010-2024 with twice-daily morning and afternoon acquisitions. The spatial resolution was evaluated to ~30 km, a 30 % enhancement compared to the SMOS L3TB at 40° and almost a 50 % enhancement compared to the SMOS L3TB at 52.5°. Then, we applied a melt detection algorithm to both the enhanced resolution product at 40° and the L3TB product at 52.5° which is used in the literature. The spatial resolution enhancement results not only in the detection of smaller melt regions but also in a widespread increase in the annual number of melt days. This increase is larger than 30 days per year in the GrIS percolation area and on multiple Antarctic ice shelves. This is primarily due to the mix of dry and wet snow regions near the ice shelves grounding line, resulting in lower brightness temperature peaks in the SMOS L3TB product due to a large power spread. These findings highlight the dependence of melt detection in particular, and geophysical applications in general, on the spatial resolution of passive microwave observations. This study provides a new open dataset suitable to monitor melt at the surface and at depth on the two main ice-sheets.

*Keywords:* SMOS, melt, Antarctica, Greenland, resolution enhancement, rSIR

---

## 1. Introduction

Surface melt occurs each summer over a large part of the Greenland Ice Sheet (GrIS) and over the margins of the Antarctic Ice Sheet (AIS) (Picard & Fily, 2006; Mote, 2007). It contributes to the ice sheet mass balance both directly through the reduction of surface mass balance (SMB) and indirectly through the enhancement of ice

---

\*Corresponding author

33 dynamics (Otosaka et al., 2023). Over the GrIS, the widespread surface melt in summer drives the negative SMB  
34 accounting for 34% to 50% of the total mass loss (Mouginot et al., 2019; IMBIE, 2020), with an increasing trend  
35 in meltwater runoff since the 1990s (Fettweis et al., 2017; IMBIE, 2020). On the contrary, the colder and drier  
36 AIS experiences melt only over the margins and the mass loss primarily comes from ice dynamics (IMBIE, 2018;  
37 Rignot et al., 2019). Most of the meltwater produced in the AIS percolates in the snowpack or forms ponds at  
38 the surface of ice shelves (Kingslake et al., 2017; Stokes et al., 2019), while runoff to the ocean is very low. When  
39 refreezing, meltwater creates impermeable ice layers which foster again the formation of supraglacial lakes.  
40 Melt ponds play a role in hydrofracturing, potentially leading to the destabilization of ice shelves (Scambos  
41 et al., 2000), and are known to have triggered the collapses of the Larsen A and B ice shelves in 1995 and 2002  
42 (Rott et al., 1996; Scambos et al., 2004; Banwell et al., 2013) and of the Wilkins ice shelf in 2008 (Scambos et al.,  
43 2009). An important consequence is the acceleration of outlet glaciers that are not anymore buttressed by their  
44 downstream ice shelves (Rott et al., 2002; Scambos et al., 2004).

45 Remote sensing is a suitable tool for detecting the presence of liquid water in the snowpack at large scale. Mi-  
46 crowave radiometers have provided a near twice-daily coverage of polar regions since 1988 and every other days  
47 since 1979, combining the Scanning Multichannel Microwave Radiometer (SMMR), Special Sensor Microwave  
48 Imager (SSM/I), Special Sensor Microwave Imager Sounder (SSMIS) and Advanced Microwave Scanning Ra-  
49 diometer (AMSR-E and AMSR2) sensors. The time series of 19 GHz and 37 GHz brightness temperatures ( $T_B$ )  
50 were used to detect wet snow occurrence and compute trends and anomalies for up to four decades (Zwally &  
51 Fiegles, 1994; Abdalati & Steffen, 1995; Torinesi et al., 2003; Liu et al., 2006; Picard & Fily, 2006; Picard et al., 2007;  
52 Tedesco, 2007; Tedesco & Fettweis, 2020). Active microwave sensors are also suitable for wet snow detection,  
53 with Synthetic Aperture Radars (SAR) such as Sentinel-1 at C-band (Liang et al., 2021), and scatterometers such  
54 as the Quik Scatterometer (QuikSCAT) at Ku-band (Ashcraft & Long, 2006; Trusel et al., 2012) and the Advanced  
55 Scatterometer (ASCAT) at C-band (Bevan et al., 2018; Kuipers Munneke et al., 2018). Lastly, optical sensors can  
56 detect the accumulation of meltwater at the surface when it forms slush, ponds and streams (Yang & Smith,  
57 2013; Bell et al., 2017; Williamson et al., 2018; Banwell et al., 2019).

58 The difference between the imaginary part of the permittivity of ice and water (related to absorption) is  
59 responsible for a large increase in the  $T_B$  at any microwave frequency when liquid water appears in snow (Zwally,  
60 1977; Picard et al., 2022). Multiple algorithms have been proposed in the past 30 years for detecting melt, with  
61 most of them being based on simple thresholding methods (Zwally & Fiegles, 1994; Abdalati & Steffen, 1995;  
62 Ramage & Isacks, 2002; Torinesi et al., 2003; Picard & Fily, 2006; Tedesco, 2007). All these algorithms use the 19  
63 GHz and 37 GHz signals to detect liquid water in the first meter of the snowpack (Picard et al., 2022). However,  
64 lower frequencies can provide additional insights on the presence of meltwater percolating into the firn.

65 The European Space Agency (ESA) Soil Moisture and Ocean Salinity (SMOS, Kerr et al. (2001)) and the Na-  
66 tional Aeronautics and Space Administration (NASA) Soil Moisture Active and Passive (SMAP, Entekhabi et al.  
67 (2010)) satellites have provided  $T_B$  at L-band (1.4 GHz) since 2010 and 2015, respectively. Both have been recently

68 used to detect melt (Leduc-Leballeur et al., 2020; Mousavi et al., 2022) and can be used in synergy with higher  
69 frequency sensors such as SSMIS or AMSR2 (Colliander et al., 2022, 2023). Both sensors are mostly limited by  
70 a coarse instrumental spatial resolution. For SMOS, the spatial resolution varies within the field of view from  
71  $\sim 30$  km to  $\sim 60$  km depending on the incidence angle, with an average resolution of 43 km (Kerr et al., 2010).  
72 SMAP radiometer achieves a comparable resolution with a 3 dB instantaneous field of view of  $39 \text{ km} \times 47 \text{ km}$   
73 (Piepmeier et al., 2017). For both sensors, the resolution of gridded  $T_B$  products is worse than the instrumental  
74 resolution, and is not sufficient to capture small-scale melt patterns observed for instance on the Shackleton  
75 (Saunderson et al., 2022) and Larsen C (Luckman et al., 2014) ice shelves. Hence, the melt detection algorithm  
76 for SMOS presented in Leduc-Leballeur et al. (2020) is based on the SMOS Level 3  $T_B$  (L3TB) product at  $52.5^\circ$   
77 incidence angle with a 25 km grid sampling, but its effective spatial resolution is coarser than 50 km.

78 This study presents the first resolution enhancement of SMOS brightness temperatures and its application  
79 to detect melt on the Antarctic and Greenland Ice Sheets. The methodology applies to the SMOS Level 1C (L1C)  
80 data a state-of-the-art image reconstruction algorithm widely used with conventional radiometers including  
81 SMAP (Long & Daum, 1998; Long & Brodzik, 2016; Long et al., 2019). Furthermore, we have taken advantage  
82 of SMOS multi-incidence capabilities to reconstruct three distinct products. The first one is the *Single-incidence*  
83 *Enhanced Resolution* dataset at  $52.5^\circ$  (SiER<sub>52.5</sub>), and uses the measurements in the  $50^\circ - 55^\circ$  incidence bin to com-  
84 pare with the L3TB at  $52.5^\circ$ . The second one is a similar dataset computed using the  $37.5^\circ - 42.5^\circ$  incidence bin  
85 (SiER<sub>40</sub>), at SMAP looking angle, where the native spatial resolution of SMOS observations is better. The third  
86 dataset, called *Multi-incidence Enhanced Resolution* (MiER), uses all the measurements with an incidence angle  
87 lower than  $40^\circ$  to exploit the observations with the best native spatial resolution near nadir. For each of these  
88 new datasets, we first evaluated the effective spatial resolution and then we applied the melt detection algorithm  
89 from Leduc-Leballeur et al. (2020). Comparisons are performed against the L3  $T_B$  and melt products to highlight  
90 the major changes due to spatial resolution enhancement.

91 Section 2 presents the different datasets used as input and for validation, Section 3 presents the whole  
92 methodology, Section 4 presents the results for the spatial resolution improvement and melt detection, and  
93 finally Section 5 discusses the limitations and perspectives to this work.

## 94 **2. Data**

### 95 *2.1. SMOS Level 1C product*

96 The Microwave Imaging Radiometer using Aperture Synthesis (MIRAS) instrument onboard SMOS is an in-  
97 terferometric radiometer operating at 1.4 GHz (Kerr et al., 2010). It is composed of 69 Lightweight Cost-Effective  
98 Front-end (LICEF) receivers which are equally distributed over a central structure and three deployable arms.  
99 The signal acquired by each LICEF receiver for one SMOS snapshot is transmitted to a central processing unit  
100 that performs cross-correlation to deliver the observables. In full polarization mode, MIRAS furnishes co- and

101 cross-polarized  $T_B$  in the XY antenna frame with a 1.2 s integration time (Wu et al., 2013). Co-polarized snap-  
102 shots provide real  $T_B^{XX}$  or  $T_B^{YY}$  measurements while cross-polarized snapshots provide complex measurements  
103  $T_B^{XY} = Re(T_B^{XY}) + Im(T_B^{XY})$ . All the values of  $T_B^{XX}$ ,  $T_B^{YY}$ ,  $Re(T_B^{XY})$  and  $Im(T_B^{XY})$  are estimated at fixed positions  
104 sampled every  $\sim 15$  km in the equal-area Discrete Global Grid (DGG, Sahr et al. (2003)). Hereafter, a DGG refers  
105 to the location of these low-level SMOS measurements.

106 The SMOS L1C  $T_B$ , version 724 distributed by ESA is the single input our processing chain requires. The  
107 L1C data are distributed by half orbit, 29 per day (both ascending and descending). L1C data blocks include  
108 the  $T_B^{XX}$ ,  $T_B^{YY}$ ,  $Re(T_B^{XY})$  and  $Im(T_B^{XY})$  acquired by MIRAS in full-polarization mode along with the longitude,  
109 latitude, altitude and identifier of each DGG, the radiometric accuracy (RA), azimuth and incidence angles, the  
110 semi-minor and semi-major axes of an ellipse approximating the -3 dB footprint of a measurement, and L1C  
111 flags which are further used in Section 3.1. For the purpose of this study, we downloaded all the L1C files from  
112 April 2010 to March 2024 and we extracted the Antarctic and Greenland measurements for each track.

### 113 2.2. SMOS CATDS Level 3 Brightness Temperatures

114 The Centre Aval de Traitement des Données SMOS (CATDS) produces twice-daily, horizontal and vertical-  
115 polarized  $T_B$  maps from SMOS posted on the EASE-2 Grid at 25 km, for each  $5^\circ$  incidence angle bin ranging  
116 from  $0^\circ$  to  $65^\circ$  (Al Bitar et al., 2017). The SMOS L3TB product is obtained by averaging the L1C  $T_B$  in all the grid  
117 pixels for each incidence bin. The averaging of multiple measurements with varying footprints and independent  
118 noise results in both a lower spatial resolution and a lower radiometric noise than the L1C  $T_B$ . SMOS L3TB  
119 has been used in cryospheric studies in particular using the near-Brewster angle ( $50$ - $55^\circ$ ) (Macelloni et al., 2019;  
120 Leduc-Leballeur et al., 2020; Houtz et al., 2021). In this study, the L3TB version 331 at bins  $50$ - $55^\circ$  and  $37.5$ - $42.5^\circ$   
121 are merged on a daily basis to compare with the outputs of our processing chain (Section 3).

### 122 2.3. SMAP rSIR-Enhanced Brightness Temperatures

123 For the purpose of comparison with our new products, and especially for assessing the effective spatial  
124 resolution, we used the SMAP Radiometer Twice-Daily rSIR-Enhanced EASE-Grid 2.0 Brightness Temperatures  
125 Version 2 dataset (Long et al., 2019; Brodzik et al., 2021) distributed at the National Snow and Ice Data Center  
126 (NSIDC). This product contains morning and evening SMAP  $T_B$  posted on EASE-2 grids with a pixel spacing of  
127 3 km, 3.125 km, 9 km, 25 km, and 36 km. The resolution of SMAP instrument is still unchanged ( $\sim 40$  km) for all  
128 these datasets. The resolution enhancement is based on the same rSIR algorithm that we used in this study for  
129 SMOS and that was previously applied to SSM/I, SSMIS and AMSR data (Long & Daum, 1998; Long & Brodzik,  
130 2016). Only the number of iterations differs. We downloaded the SMAP rSIR-enhanced, Version 2 3.125 km  $T_B$   
131 maps for two particular events lasting three days each where the spatial resolution is evaluated (Section 3.4). A  
132 single 12.5 km SMOS L1C rSIR-enhanced pixel therefore contains 16 SMAP rSIR-enhanced pixels.

133 2.4. Sentinel-1 images

134 We used images from the ESA Sentinel-1 SAR Ground Range Detected (GRD) product in the process of  
 135 quantifying the effective spatial resolution of the SMOS enhanced-resolution maps. Two sets of images were  
 136 chosen: the first one is over Anvers Island ( $-64.5^\circ$  latitude,  $-63.5^\circ$  longitude) in the Antarctic Peninsula (AP) on the  
 137 26<sup>th</sup> of January 2019, and the second one is over West ice-shelf ( $-66.5^\circ$  latitude,  $83^\circ$  longitude) in East Antarctica  
 138 on the 8<sup>th</sup> of February 2019. We preprocessed and downloaded HV backscatter images using the Google Earth  
 139 Engine (GEE) code editor. Preprocessing steps include the thermal noise removal, radiometric calibration and  
 140 terrain correction as implemented in the Sentinel-1 toolbox.

141 3. Methods

142 The methodology is depicted in Figure 1 and the steps are presented in the following sections.

143 3.1. Conversion of  $T_B$  to the surface frame and preprocessing

144 The preprocessing applied to SMOS L1C data consists in four steps: i) conversion of the  $T_B$  from the (XY)  
 145 antenna frame to the (HV) surface frame, ii) removal of the low-quality and flagged L1C data, iii) incidence  
 146 angle binning and selection, and iv) solar time calculation.

147 The first step provides linearly polarized  $T_B$  defined in the surface frame with its vertical and horizontal  
 148 components. These are used by most geophysical applications over the ice sheets, such as the melt detection  
 149 and ice sheet temperature estimation algorithms based on the horizontal and vertical polarization, respectively  
 150 (Leduc-Leballeur et al., 2020; Macelloni et al., 2019). Hence, the sequences of  $T_B^{XX}$ ,  $T_B^{YY}$ ,  $Re(T_B^{XY})$  and  $Im(T_B^{XY})$   
 151 measurements given in L1C data are first converted to  $(T_B^H, T_B^V)$  pairs. The conversion from the HV surface  
 152 frame to the XY antenna frame is a simple rotation that requires as input the geometrical and Faraday angles,  
 153 and the inverse operation needed here converts a sequence of measurements  $[T_B^{XX}, T_B^{YY}, Re(T_B^{XY}), Im(T_B^{XY})]$  to  
 154 the fully-polarized  $[T_B^H, T_B^V, 3^{rd}$  and  $4^{th}$  Stokes components]. We first construct the vector  $[T_B^{XX}, T_B^{YY}, Re(T_B^{XY}),$   
 155  $Im(T_B^{XY})]$  for each snapshot, with one exact value and three values obtained through the interpolation of a

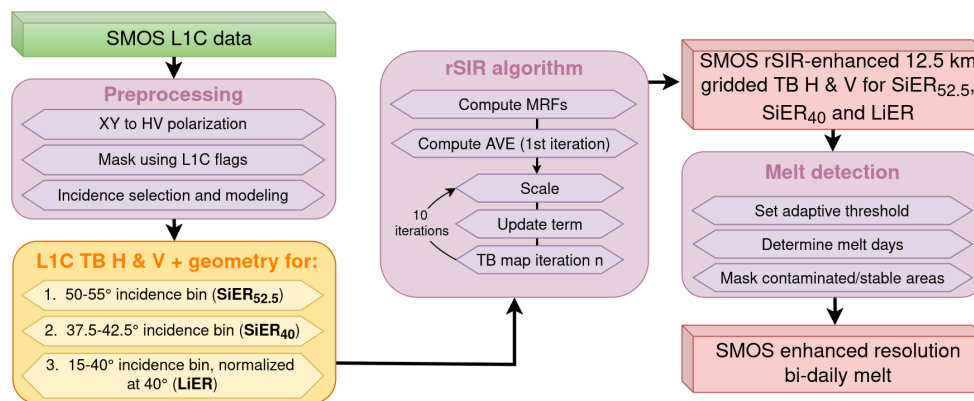


Figure 1: Flowchart of the SMOS resolution-enhancement and melt detection algorithms. The output datasets are highlighted in red boxes.

156 sequence of close measurements with limited incidence angle variations. The  $T_B^H$  and  $T_B^V$  in surface frame are  
157 then obtained through inversion of the rotation matrix.

158 In the second step, we discarded the data affected by sun aliases, radio frequency interferences (RFI) and  
159 the observations located in the aliased area of a snapshot, as the image reconstruction algorithm is particularly  
160 sensitive to noise. For this, we discarded data with the L1C flags (ESA, 2021): *sun point*, *sun glint area*, *alias-free*  
161 *field of view*, *border field of view*, *RFI*, *RFI tails* and *RFI amplitude*. As we noticed additional noise in Greenland  
162 that may be due to an incorrect RFI filtering, we also discarded all the observations with a non-physical  $T_B$   
163 higher than 280 K.

164 In the third step, we selected different ranges of incidence angle to compute three SMOS enhanced-resolution  
165 datasets. The motivation is the large dependence of SMOS L1C spatial resolution on the incidence angle (Fig-  
166 ure 2a). The ellipse approximating the -3 dB footprint is larger and more eccentric at higher incidences. The  
167 semi-major axis is <20 km for an incidence <20° while it is ~40 km at 52.5° and reaches 90 km near 70°. A careful  
168 selection of the L1C data is therefore necessary to obtain an optimum spatial resolution. The first two enhanced-  
169 resolution datasets use the observations in a short range of incidences (5°) centered at 52.5° (Single-incidence  
170 Enhanced Resolution, SiER<sub>52.5</sub>) near the Brewster angle, and 40° (SiER<sub>40</sub>, at SMAP looking angle), respectively.  
171 These incidence bins exist in the L3TB product leading to an easy evaluation of the gain in spatial resolution.  
172 The third dataset uses all the observations with an incidence angle lower than 40° (Multi-incidence Enhanced  
173 Resolution, MiER). It is designed to exploit the near-nadir observations owing the best native spatial resolution.  
174 The low-incidence measurements (<40°) correspond to the dark blue dots and the red contour in Figure 2.

175 Figure 2c shows the variations of the radiometric accuracy in H pol ( $RA_H$ ) within a SMOS snapshot (~1500  
176 × 1500 km<sup>2</sup>).  $RA_H$  is around 2 K at boresight and is degraded up to 8-9 K along the margins of the snapshot,  
177 especially in the cross-track direction. The  $RA_H$  is low in the entire area covered once the flagged observations  
178 have been discarded, that is in medium blue in Figure 2b, and also after the 40° incidence selection (red contour  
179 in Figure 2b). The selected observations therefore have a low noise to facilitate the image reconstruction process.

180 Finally, we separated the morning (before 12 A.M.) and afternoon measurements according to their local  
181 solar time which is calculated as  $t_{\text{solar}} = t_{\text{UTC}} + \text{longitude}/15$ . Morning and afternoon measurements correspond  
182 broadly to the ascending and descending passes, respectively.

### 183 3.2. Modeling the incidence angle variations

184 To accommodate the large range of incidence in the MiER product, we devised a normalization procedure  
185 of the  $T_B$  to a common equivalent angle, chosen at 40° by convention and for comparability with SMAP. For  
186 this, we first modeled the angular variations through a semi-physical approach and then applied this model  
187 to scale the  $T_B$  at 40° incidence. The Multi-Fresnel Thermal Emission (MFTE) model described in detail in Ap-  
188 pendix A computes the upwelling radiation emanating from a stack of snow layers with uniform temperature  
189 and alternating density values. Given the permittivities  $\epsilon_1$  and  $\epsilon_2$  of the alternating layers computed from the  
190 density values, the model calculates the reflection coefficients in H and V polarizations ( $R_H$ ,  $R_V$ ). The modeled

191 brightness temperatures  $T_{B,\text{model}}^{\text{H}}$  and  $T_{B,\text{model}}^{\text{V}}$  are then calculated as:

$$T_{B,\text{model}}^{\text{H}} = T(1 - R_H) \quad (1)$$

192

$$T_{B,\text{model}}^{\text{V}} = T(1 - R_V) \quad (2)$$

193 After a first evaluation, we found that this simple physical model does not perfectly reproduce SMOS in-  
 194 cidence diagrams. As an example, Figure 3 presents the morning and afternoon  $T_{\text{B}}^{\text{H}}$  and  $T_{\text{B}}^{\text{V}}$  acquired around  
 195 Dome C in Antarctica for a single day, as a function of the incidence angle. The dashed lines in Figure 3 were  
 196 obtained using the MFTE model after fitting both density values. In particular, we note that the model con-  
 197 strains  $T_{B,\text{model}}^{\text{H}}(0^\circ) = T_{B,\text{model}}^{\text{V}}(0^\circ)$ , for physical reasons while SMOS features significantly lower  $T_{\text{B}}^{\text{H}}$  values at low  
 198 incidence and a steeper variation in  $T_{\text{B}}^{\text{V}}$  than the physical model does. To add flexibility in the model, we added  
 199 an empirical linear term to Equation (1), giving:

$$T_{B,\text{model}}^{\text{H}} = T(1 - R_H)(\beta + \alpha(1 - \cos\theta)) \quad (3)$$

200 where the coefficients  $\alpha$  and  $\beta$  are unknown. In this case, five unknown parameters need to be estimated:  $\epsilon_1$ ,  
 201  $\epsilon_2$ ,  $T$ ,  $\alpha$  and  $\beta$ . Note that the physical model is obtained for  $\alpha = 0$  and  $\beta = 1$ . The solid curves in Figure 3  
 202 represent the incidence diagrams in Dome C that were computed using the semi-physical model. The constraint  
 203 at  $0^\circ$  incidence angle is relaxed which allows the model to represent the incidence diagram without bias. We  
 204 assessed the robustness of this semi-physical model by visual inspections in numerous cases, including over ice  
 205 shelves in both winter and summer. Because our purpose is to normalize SMOS L1C  $T_{\text{B}}$  without introducing a  
 206 bias, which was the case using the physical model only, we adopted the semi-physical approach to compute the  
 207 MiER product.

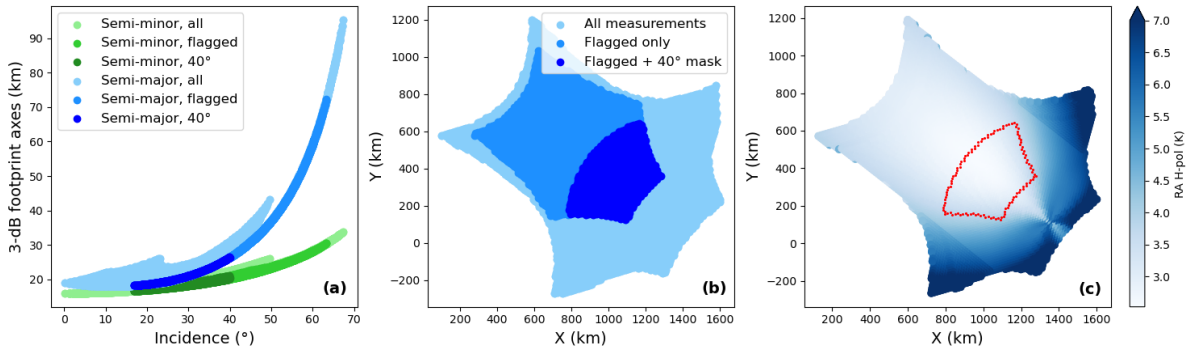


Figure 2: Overview of the L1C flags, radiometric accuracy ( $RA_H$ ) and spatial resolution variations for one SMOS snapshot on the 19<sup>th</sup> of January, 2019. (a) Scatterplot of the semi-minor and semi-major axes of the -3 dB antenna footprint against the incidence angle. The light blue and green curves represent all the observations. The medium blue and green curves show the remaining observations once the flagged L1C data have been discarded. The dark blue and green curves show the observations with an incidence  $<40^\circ$ . (b) Location of the non-flagged (remaining) data and the observations with incidence  $<40^\circ$  within the snapshot, and (c) Spatial distribution of  $RA_H$  within the snapshot with the contour of the  $<40^\circ$  measurements in red.



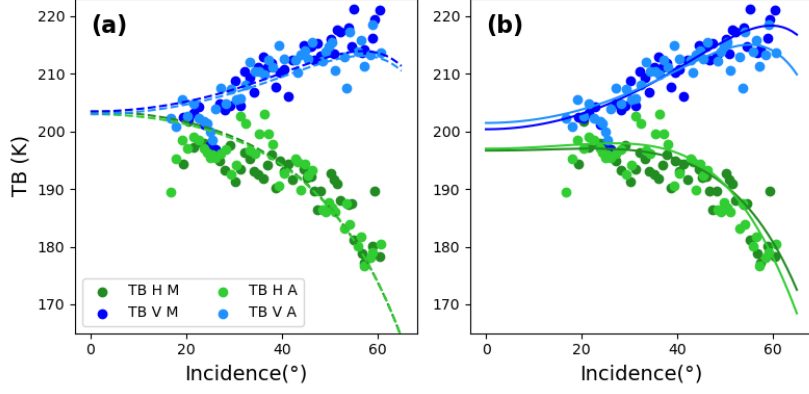


Figure 3: Observed and modeled brightness temperatures as a function of the incidence angle over the DGG n°7144462 close to Dome C on the 19th of January, 2019 for the morning (M) and afternoon (A) passes. In (a) the physical multilayer model was fitted to H and V polarized  $T_B$ . (b) is the same for the semi-physical model that includes a linear correction term at H polarization.

208 Finally, the normalization of SMOS brightness temperatures for the MiER product was performed as follows:

$$T_B^p(40^\circ) = T_B^p \frac{T_{B,model}^p(40^\circ)}{T_{B,model}^p} \quad (4)$$

209 where  $p$  is the polarization. For convenience, the reference angle is set to  $40^\circ$ , to facilitate the comparison with  
 210 SMAP which has a fixed incidence angle of  $40^\circ$ .

### 211 3.3. rSIR algorithm

212 To retrieve SMOS enhanced resolution  $T_B$ , we applied the radiometer version of the Scatterometer Image  
 213 Reconstruction (rSIR) algorithm following Long & Daum (1998) with a few adaptations. This algorithm has been  
 214 widely used within the framework of the National Aeronautics and Space Administration (NASA) Making Earth  
 215 System Data Records for Use in Research Environments (MEaSUREs) program to compute enhanced resolution  
 216  $T_B$  products from SSM/I, SSMIS, AMSR and SMAP on equal-area grids (Long & Brodzik, 2016; Long et al., 2019).

217 First, the algorithm requires an approximation of the spatial Measurement Response Function (MRF) which  
 218 represents the smeared antenna gain pattern projected on Earth's surface for every single measurement. Fol-  
 219 lowing previous literature (Long & Brodzik, 2016; Brodzik & Long, 2018) and assuming the response is a two-  
 220 dimensional Gaussian where a half-power point corresponds to the -3 dB footprint contour, the discrete MRF  
 221 (in dB) of an observation  $T_i$  is computed in each pixel  $p(x, y)$  as:

$$\text{MRF}_i(x, y) = \ln \left( \frac{1}{2} \right) \exp \left( \left( \frac{2 D_x}{a} \right)^2 + \left( \frac{2 D_y}{b} \right)^2 \right) \quad (5)$$

222 where  $a$  is the semi-major axis and  $b$  the semi-minor axis of an ellipse approximating the 3-dB antenna foot-  
 223 print.  $D_x$  and  $D_y$  are the relative distances from the footprint center to each pixel taken along and across the  
 224 orientation of the ellipse, respectively. This model was found to be adequate for further image reconstruction  
 225 processes (Long, 2015).

226 For each polarization  $p$ , we consider a measurement  $T_i^p$  as the sum of the brightness temperature  $T_B^p$  sampled

227 on the Earth's surface weighted by the MRF:

$$T_i^p = \iint \text{MRF}_i(x, y) T_B^p(x, y) dx dy \quad (6)$$

228 The image reconstruction approach in rSIR algorithm aims to estimate the discrete  $T_B^p(x, y)$  image from a set of  
 229 radiometer measurements  $T_i^p$  using the modeled  $\text{MRF}_i$ . Let  $a_j$  be the estimated  $T_B^p(x_j, y_j)$  of the row-scanned  
 230  $j$ -th pixel. The initialization of the algorithm is performed as a weighted average called AVE:

$$\text{AVE} = a_j^0 = \frac{\sum_i \text{MRF}_{ij} T_i}{\sum_i \text{MRF}_{ij}} \quad (7)$$

231 Then, for every iteration  $k$  the algorithm determines the estimated brightness temperature  $a_j^{k+1}$  as:

$$f_i^k = \frac{\sum_n \text{MRF}_{in} a_n^k}{\sum_n \text{MRF}_{in}} \quad (8)$$

232

$$d_i^k = \sqrt{T_i / f_i^k} \quad (9)$$

233

$$u_{ij}^k = \begin{cases} \left[ \frac{1}{2f_i^k} \left( 1 - \frac{1}{d_i^k} \right) + \frac{1}{a_j^k d_i^k} \right]^{-1}, & d_i^k \geq 1 \\ \left[ \frac{1}{2} f_i^k \left( 1 - d_i^k \right) + a_j^k d_i^k \right], & d_i^k < 1 \end{cases} \quad (10)$$

234

$$a_j^{k+1} = \frac{\sum_i \text{MRF}_{ij} u_{ij}^k}{\sum_i \text{MRF}_{ij}} \quad (11)$$

235 where  $f_i^k$  is called the forward projection,  $d_i^k$  is the scale factor and  $u_{ij}^k$  is the update term (Long & Daum, 1998).

236 This process is iterated  $K$  times. Long & Daum (1998); Long & Brodzik (2016) noticed that both the recon-  
 237 struction accuracy and the noise level increase while iterating.  $K$  was set to 10 iterations in our algorithm as this  
 238 value permits a good tradeoff between noise and reconstruction accuracy. It is lower than the 20 iterations used  
 239 for SSM/I in Long & Brodzik (2016) to account for the higher noise in the interferometric MIRAS measurements  
 240 compared to conventional radiometers ( $\sim 2$  K vs  $< 1$  K typically). After 10 iterations, the reconstruction accuracy  
 241 converges towards an asymptotic value with few changes compared to 15 or 20 iterations (also evaluated), while  
 242 the noise level is increasing rapidly.

243 The enhanced-resolution  $T_B$  maps were computed the same way for both H and V polarizations and morning  
 244 and afternoon passes over the entire 14-year SMOS dataset, for the SiER<sub>52.5</sub>, SiER<sub>40</sub> and MiER products.

#### 245 3.4. Evaluation of the effective spatial resolution

246 We defined a common methodology to evaluate and compare the effective spatial resolution of six datasets:  
 247 the three new SMOS rSIR-enhanced datasets based on the L1C data (SiER<sub>52.5</sub>, SiER<sub>40</sub> and MiER), the SMAP  
 248 rSIR-enhanced  $T_B$  and the SMOS L3TB at both 52.5° and 40° incidence angles. The effective spatial resolution is  
 249 defined here as the Full Width at Half Maximum (FWHM) of the Pixel Spatial Response Function (PSRF), which

250 is modeled as a two-dimensional Gaussian. The FWHM is related to the standard deviation  $\sigma$  of the Gaussian  
251 through:

$$\text{FWHM} = 2 \sqrt{2 \ln(2)} \sigma \approx 2.355 \sigma \quad (12)$$

252 To determine the FWHM for each dataset, we first identified a suitable region with an abrupt and large spatial  
253 transition, such as between the ice-sheet and the ocean. This transition is modeled as a two-dimensional step  
254 function. The convolution of 2D Gaussian kernels of varying FWHM with this step function is compared to  
255 the observed  $T_B$  to determine the smoothness of brightness temperature changes. We minimize the Root Mean  
256 Square Error (RMSE) between the convoluted and observed data to find the optimal FWHM corresponding to the  
257 estimated spatial resolution. The RMSE was computed along a transect perpendicular to the coastline instead  
258 of the whole image.

259 The step function is defined here using Sentinel-1 HV images to delineate the ice and ocean surfaces which  
260 correspond to the maximum and minimum expected brightness temperatures, respectively (see Figure 4, left  
261 column). Two case studies are investigated, over the western Antarctic Peninsula on January 26<sup>th</sup>, 2019 and over  
262 West ice shelf in East Antarctica on February 8<sup>th</sup>, 2019.

### 263 3.5. Liquid water detection

264 The presence of liquid water in the snowpack is detected using the adaptive-threshold algorithm published  
265 in Leduc-Leballeur et al. (2020) with very few changes. This algorithm for SMOS stems from an earlier algorithm  
266 designed for 19 GHz observations acquired by SMMR and SSM/I (Torinesi et al., 2003), and further improved by  
267 Picard & Fily (2006) with successful applications to SSMIS, AMSR-E and AMSR2 (e.g. (Saunders et al., 2022)).

268 In brief, the sharp increase in  $T_B$  time series caused by the liquid water appearance is detected using a  
269 threshold value computed as:

$$T = M + 3 \times \sigma \quad (13)$$

270 where  $M$  is the average and  $\sigma$  is the standard deviation of  $T_B^H$  calculated in dry snow days only, from the 1<sup>st</sup> of  
271 April to the 31<sup>st</sup> of March. The problem is circular as the knowledge of melt days is required to exclude them  
272 from the computation of  $M$  and  $\sigma$ , which are further used to detect melt. This is resolved by first detecting melt  
273 using the all-day annual average for  $M$  and a fixed value of 15 K for  $3\sigma$ . The first-guess melt time series is then  
274 used to update  $M$  and  $\sigma$ . Three iterations are performed to obtain the definitive threshold, used to compute the  
275 final melt time-series.

276 Noting that false alarms occur in the interior of the Antarctic ice-sheet where melt is obviously absent, we  
277 identified and masked these areas by excluding the pixels where the standard deviation of  $T_B^V$  exceeds 2.8 K,  
278 following Leduc-Leballeur et al. (2020). As this threshold was optimized for Antarctica, it was reevaluated and  
279 set to 5 K on Greenland where we noticed a higher variability in SMOS  $T_B$  time series.

280 In Antarctica, coastal pixels also show frequent false alarms due to ocean contamination of the radiometric  
281 signal. The higher  $T_B$  on sea-ice than on open ocean indeed leads to a large and erroneous detection of winter

Table 1: Average percentage of the AIS pixels revisited in one or two days for the MiER, SiER<sub>40</sub> and SiER<sub>52.5</sub> products. The coverage was evaluated for morning and afternoon tracks separately, and also for the daily average of all the tracks.

		<b>rSIR morning</b>	<b>rSIR afternoon</b>	<b>rSIR daily</b>
<b>1-day coverage (%)</b>	<b>MiER</b>	90.1	91.1	98.0
	<b>SiER<sub>40</sub></b>	93.7	94.5	99.2
	<b>SiER<sub>52.5</sub></b>	92.2	93.3	98.6
<b>2-day coverage (%)</b>	<b>MiER</b>	99.4	99.7	99.9
	<b>SiER<sub>40</sub></b>	99.6	99.7	100.0
	<b>SiER<sub>52.5</sub></b>	99.3	99.6	99.7

282 melt days along the coastlines. Winter melt may occur on multiple Antarctic ice shelves due to foehn wind  
 283 (Kuipers Munneke et al., 2018) or atmospheric rivers (Wille et al., 2019), but with much lower recurrence. Hence,  
 284 we computed a contamination mask over Antarctica that filters out the pixels where the winter melt occurrence  
 285 overpasses 5 % in the entire 14-year melt time series. In Greenland, where winter melt is more frequent, the  
 286 contamination mask is not needed due to the much lower number of marine-terminating glaciers.

## 287 4. Results

288 We produced three twice daily SMOS rSIR-enhanced datasets based on the L1C product for the period 2010-  
 289 2024: the SiER<sub>52.5</sub>, SiER<sub>40</sub> and MiER. The coverage of these datasets and the radiometric comparison against the  
 290 SMOS L3TB product are first presented. Then, we evaluate the spatial resolution of each product in two case  
 291 studies. Finally, we apply the melt detection algorithm and analyze the benefit of the resolution enhancement  
 292 for this application.

### 293 4.1. SMOS rSIR-enhanced products

294 Table 1 presents the percentage of Antarctic pixels revisited every day and at least every two days for the  
 295 SiER<sub>52.5</sub>, SiER<sub>40</sub> and MiER datasets. The revisit was computed for the daily average of all tracks and for morning  
 296 and afternoon tracks separately throughout one year (2019). For the three evaluated datasets, the morning and  
 297 afternoon tracks cover each more than 90 % of the AIS within one day and >99 % of the AIS within two days.  
 298 Hence, the SMOS rSIR-enhanced datasets are suitable to detect daily or sub-daily  $T_B$  variations associated to a  
 299 melt signal.

300 The radiometric quality of the SMOS rSIR-enhanced datasets was evaluated by comparing to the 40° and  
 301 52.5° incidence bins of the L3TB product. Table 2 presents the bias and the Root Mean Square Deviation (RMSD)

Table 2: Bias and Root Mean Square Deviation (RMSD) over 1 year (2019) between the SMOS rSIR-enhanced datasets and the SMOS L3TB at both 40° (MiER, SiER<sub>40</sub>) and 52.5° (SiER<sub>52.5</sub>) incidence angle over Antarctica and Greenland. All units are in Kelvin (K).

		<b>bias H</b>	<b>bias V</b>	<b>RMSD H</b>	<b>RMSD V</b>
<b>Antarctica</b>	<b>MiER</b>	1.60	-0.97	3.15	2.68
	<b>SiER<sub>40</sub></b>	0.75	0.41	2.91	2.40
	<b>SiER<sub>52.5</sub></b>	-0.07	0.08	2.23	1.71
<b>Greenland</b>	<b>MiER</b>	1.16	-0.64	3.86	3.60
	<b>SiER<sub>40</sub></b>	0.41	0.31	3.90	3.42
	<b>SiER<sub>52.5</sub></b>	-0.02	0.33	3.10	2.64

302 computed over Antarctica and Greenland in 2019 for all the pairs of datasets compared. We expect a low bias  
 303 as an indicator of the consistency of each dataset, and a RMSD very low on the stable areas of the Antarctic  
 304 plateau but much higher on the periphery of the ice sheet where most of the differences due to the resolution  
 305 enhancement are concentrated. Compared to the L3TB product at  $40^\circ$ , the results show a higher bias for the  
 306 MiER (+1.16 K to +1.6 K for H, -0.64 K to -0.97 K for V) than for the SiER<sub>40</sub> (<0.75 K). The SiER<sub>52.5</sub> dataset also  
 307 shows a low bias compared to the L3TB product at  $52.5^\circ$  (<0.33 K). For all the datasets, we obtain a consistent  
 308 RMSD between 2 K and 4 K with most of the differences concentrated near the coastlines. Only the MiER shows  
 309 a systematic bias in the dry and homogeneous Antarctic plateau, which may indicate issues in the incidence  
 310 diagram modeling. None of the incidence diagrams inspected show an anomalous pattern, but numerical issues  
 311 in the least square fit could lead to find a wrong local minimum.

#### 312 4.2. Evaluation of the effective spatial resolution

313 The effective spatial resolution is evaluated in two case studies presented in Figure 4: the West ice shelf (East  
 314 Antarctica, top row) and the Anvers Island (Antarctic Peninsula, bottom row). The first column shows the 2D  
 315 land/ocean step function derived from Sentinel-1 and the other columns show four  $T_B^V$  maps at  $40^\circ$  incidence:  
 316 the SMAP rSIR-enhanced from Long et al. (2019), the SMOS rSIR-enhanced MiER ( $15-40^\circ$ ) and SiER<sub>40</sub> ( $40^\circ$ ), and  
 317 the SMOS L3TB. We normalized the  $T_B^V$  maps between 0 and 1 to compare measurements performed by different  
 318 sensors. Qualitatively, the spatial resolutions of the SMAP enhanced and the two SMOS enhanced maps look  
 319 similar although the grid is four times finer in SMAP (3.125 km against 12.5 km). The SMOS L3TB at  $40^\circ$  shows a  
 320 larger land-ocean transition indicating a lower spatial resolution in both case studies. For instance, the local  $T_B$   
 321 maximums at the locations of Anvers and Brabant islands as well as the channel separating these islands from

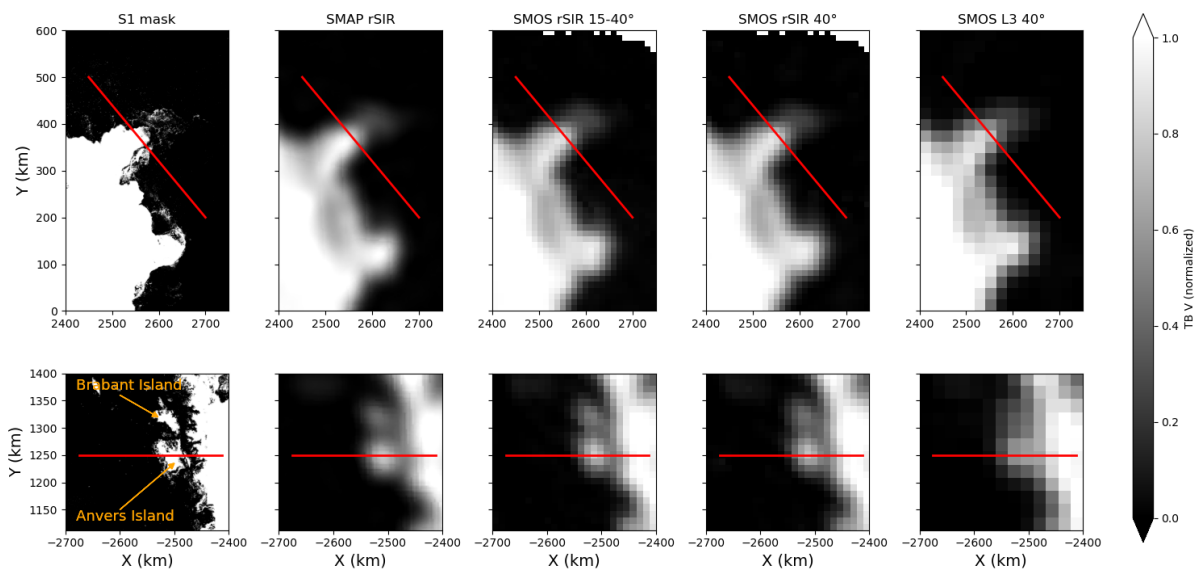


Figure 4: Normalized  $T_B^V$  for the ideal S1 mask, SMAP rSIR-enhanced evening tracks, SMOS rSIR-enhanced multi-incidence ( $15-40^\circ$ ) and single-incidence ( $40^\circ$ ) afternoon passes and SMOS daily L3TB products over the West ice-shelf on February 7-9<sup>th</sup>, 2019 (top row) and over Anvers Island on January 25-27<sup>th</sup>, 2019 (bottom row). The red lines show the transects used to compute the effective spatial resolution of each product in Figure 5.

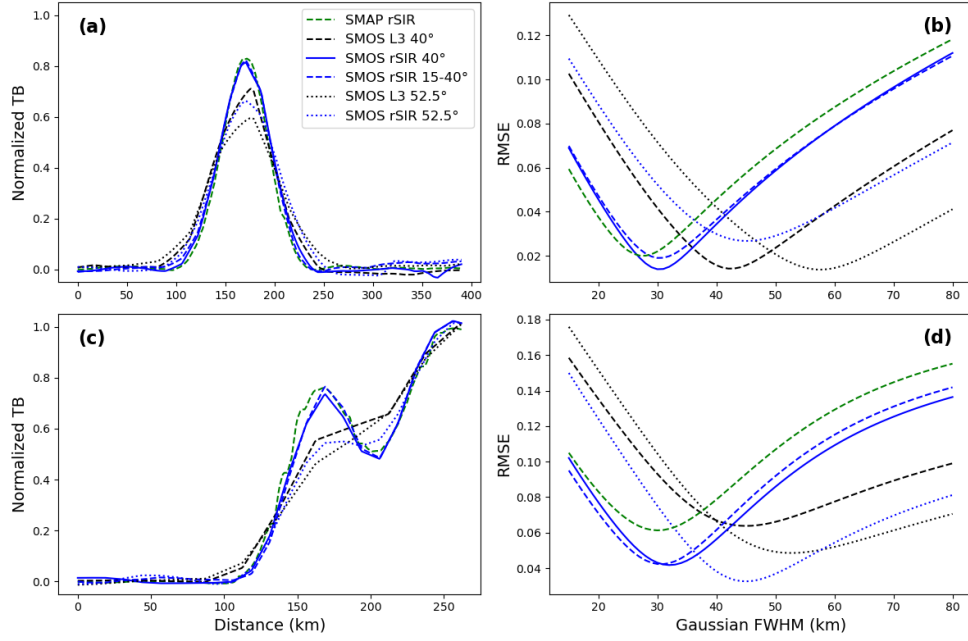


Figure 5: Estimation of the effective spatial resolution along two transects for the West ice shelf (a, b) and Anvers Island (c, d) case studies (see Figure 4 for the locations of these transects). (a, c)  $T_B$  plotted along the transects, (b, d) RMSE between the observed and convoluted images plotted against the FWHM of Gaussian kernels used for convolution. The estimated effective spatial resolutions are the FWHM at minimum RMSE for each dataset.

322 the continent are well identified in all the SMAP rSIR and SMOS rSIR products. These features are smoothed in  
 323 the SMOS L3TB where a continuous gradient from ocean to land is rather observed.

324 Quantitatively, the spatial resolution was estimated along two transects (red lines in Figure 4). Figure 5  
 325 presents the normalized  $T_B^V$  along these transects (a, c), and the RMSE computed between the observed and  
 326 convoluted images as a function of the Gaussian FWHM (b, d). For all the datasets evaluated, the RMSE de-  
 327 creases until reaching a minimum where the observed and convoluted maps match the best and then increases  
 328 again. The effective spatial resolution is the FWHM at the minimum of RMSE and is reported in Table 3 for all  
 329 the six datasets and for both case studies in H and V polarizations. The results are very close for each location  
 330 and polarization showing the robustness of the estimation. The MiER, SiER<sub>40</sub> and SMAP rSIR-enhanced  $T_B$  maps  
 331 have the finer spatial resolution, around 30 km, while the SMOS L3TB at 40° has a spatial resolution of 42-47 km.  
 332 At 52.5° incidence, the SiER<sub>52.5</sub> product has a spatial resolution of 45-48 km and the SMOS L3TB is in the range  
 333 of 53-60 km. The SiER<sub>40</sub> product therefore improves the spatial resolution by 40-50 % compared to the L3TB at

Table 3: Estimated spatial resolution along two transects over the West ice-shelf and Anvers island, using six datasets: the SMOS L3TB at 52.5° and 40°, the SMOS rSIR-enhanced SiER<sub>40</sub>, SiER<sub>52.5</sub> and MiER, and the SMAP rSIR-enhanced at 40°. For each dataset both the H-pol and V-pol spatial resolution were computed.

Dataset	Spatial resolution (km)			
	Anvers H	Anvers V	West H	West V
SMOS L3TB 52.5°	55	53	60	58
SMOS L3TB 40°	47	45	44	42
SMOS rSIR 52.5°	47	45	48	45
SMOS rSIR 40°	33	32	31	30
SMOS rSIR 15-40°	33	31	33	30
SMAP rSIR	31	30	28	28

334 52.5°, half of the enhancement being due to the reconstruction algorithm (rSIR) while the other half is due to  
335 the lower incidence angle used here. Based on these results, we further used the SiER<sub>40</sub> product to assess the  
336 impact of resolution enhancement on melt detection.

337 *4.3. Impact of the resolution enhancement on melt detection*

338 *4.3.1. Ice-sheet wide comparison of melt detection*

339 We calculated the 14 year-long (April 2010 - March 2024) time series of melt in Greenland and Antarctica using  
340 the original SMOS L3TB product at 52.5° and the new rSIR-enhanced SiER<sub>40</sub> product, using the melt detection  
341 algorithm presented in Leduc-Leballeur et al. (2020) and Section 3.5. Note that twice-daily melt was computed  
342 from the rSIR-enhanced dataset while the L3TB melt only includes a daily estimation which combines morning  
343 and afternoon tracks.

344 The average annual number of melt days according to the enhanced product is shown over Antarctica in  
345 Figure 6. It is particularly high over the Antarctic Peninsula, with up to 100 days per year on average on the  
346 Wilkins ice shelf. Other regions with a large and recurrent melt signal are located all around Antarctica, on  
347 the Riiser-Larsen, Fimbul, Roi Baudoin, Amery, West, Shackleton and Abbott ice shelves. Additionally, more  
348 localized melt patterns with a lower extent and/or less than 30 melt days per year can be distinguished, for  
349 example in Wilkes Land.

350 The difference between the average annual number of melt days computed using the SiER<sub>40</sub> product and the  
351 SMOS L3TB at 52.5° is shown in Figure 7. The pink color represents regions where the enhanced dataset detects

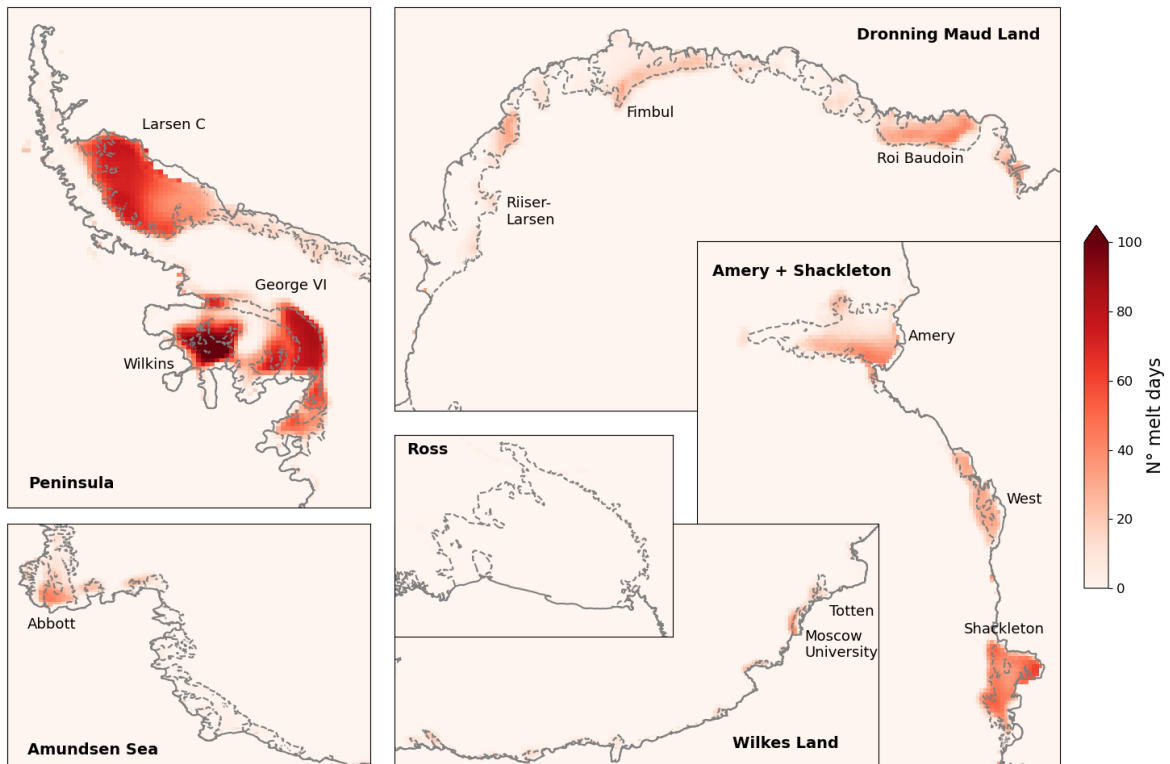


Figure 6: 2010-2024 annual average number of melt days detected using SMOS rSIR-enhanced resolution dataset over Antarctica.

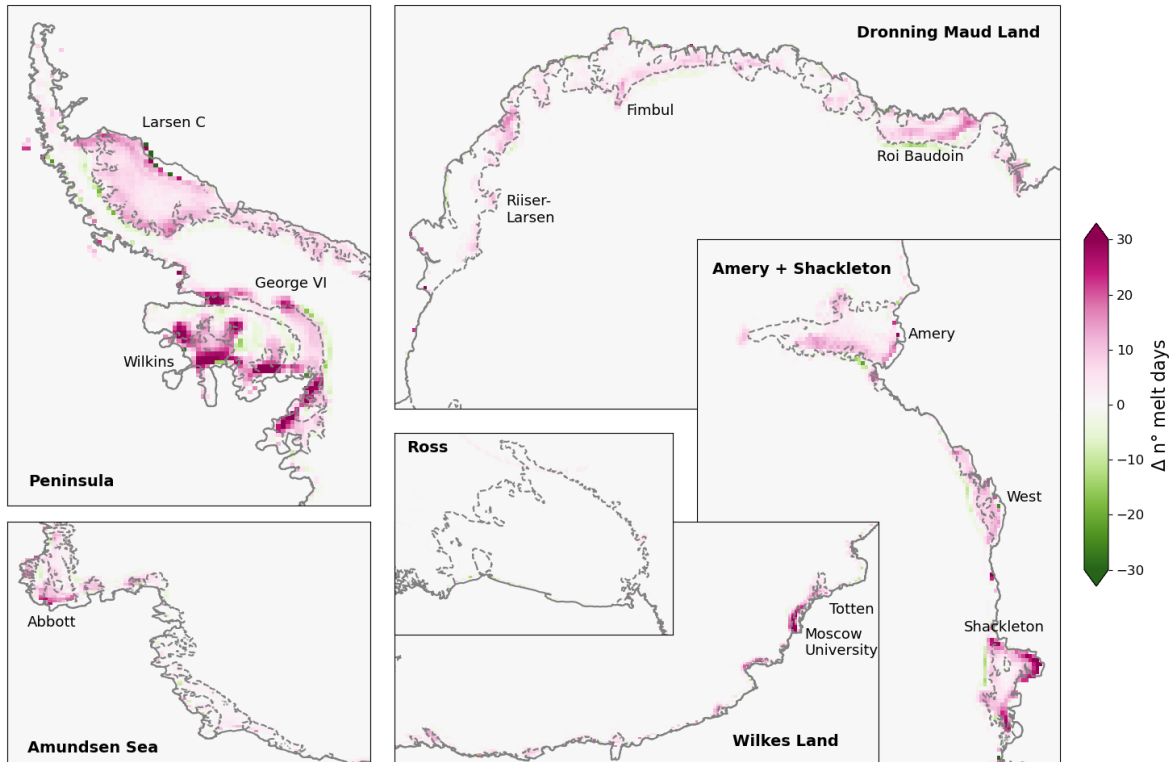


Figure 7: Difference between the 2010-2024 annual average number of melt days detected using SMOS rSIR-enhanced and SMOS L3TB datasets. A higher number of melt days in the enhanced resolution product is shown in pink.

352 more melt than the L3TB, and conversely the green color represents regions with less melt than in the L3TB.  
 353 The dominant pink color on the map clearly demonstrates that the resolution enhancement makes it possible  
 354 to capture a longer and wider melt signal over all the Antarctic ice shelves. We found above 30 additional melt  
 355 days in several regions. This is especially the case near the grounding line (dashed lines in Figure 6 and Figure 7)  
 356 where the transition from dry to wet snow is sharper in the enhanced resolution dataset. Moreover, the green  
 357 areas are often very localized above the grounding line, *e.g.* for the George VI, Larsen C, Roi Beaudoin and  
 358 Shackleton ice shelves, suggesting false-positives (i.e. over-estimation) in the L3TB due to the spreading of the  
 359 wet snow signal. We also notice that in some regions the L3TB product indicates no melt days at all, while the  
 360 enhanced resolution dataset captures more than 10 melt days per year on average, such as in Wilkes Land on  
 361 the Moscow University and Totten ice shelves.

362 The number of melt days detected by the L3TB and SiER<sub>40</sub> products over Greenland and their differences are  
 363 shown in Figure 8 for each melt year from 2010 to 2023. Several remarks can be inferred. First, when compared  
 364 to the L3TB, the SiER<sub>40</sub> melt presents similar spatial patterns with intense melt on the contour of the ice-sheet. A  
 365 large number of melt days is observed in the southeast and southwest Greenland particularly. This is coherent  
 366 with previous studies reporting the presence of perennial firn aquifers and ice slabs in these regions (Koenig  
 367 et al., 2014; Miège et al., 2016; Miller et al., 2020, 2022). The interannual variability is well represented with an  
 368 exceptional melt season in 2012 which was identified and studied in the literature (Nghiem et al., 2012).

369 Large differences between the L3TB and SiER<sub>40</sub> melt in Greenland affect most of the melting areas around



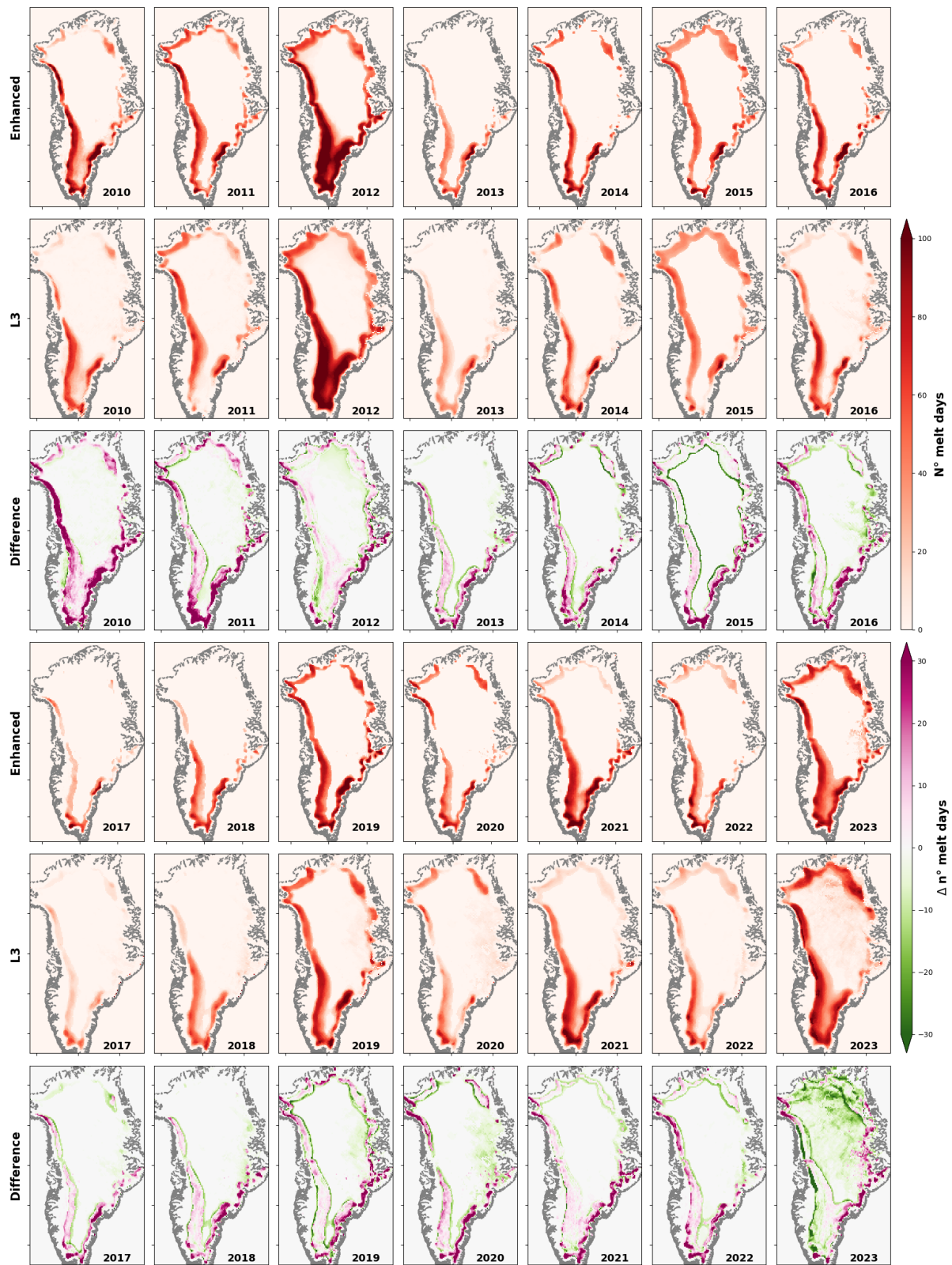


Figure 8: Annual number of melt days detected over Greenland using the SMOS MiER, L3TB and the difference between both products. Fourteen melt years from 2010-2011 to 2023-2024 are presented in the panels.

370 the ice sheet. As in Antarctica, the SiER<sub>40</sub> product consistently features a larger number of melt days (about +30)  
 371 compared to the L3TB product in many locations and especially along the southeastern coast. On the contrary,  
 372 the number of melt days is larger in the L3TB on thin bands located in the upper part of the melting regions.

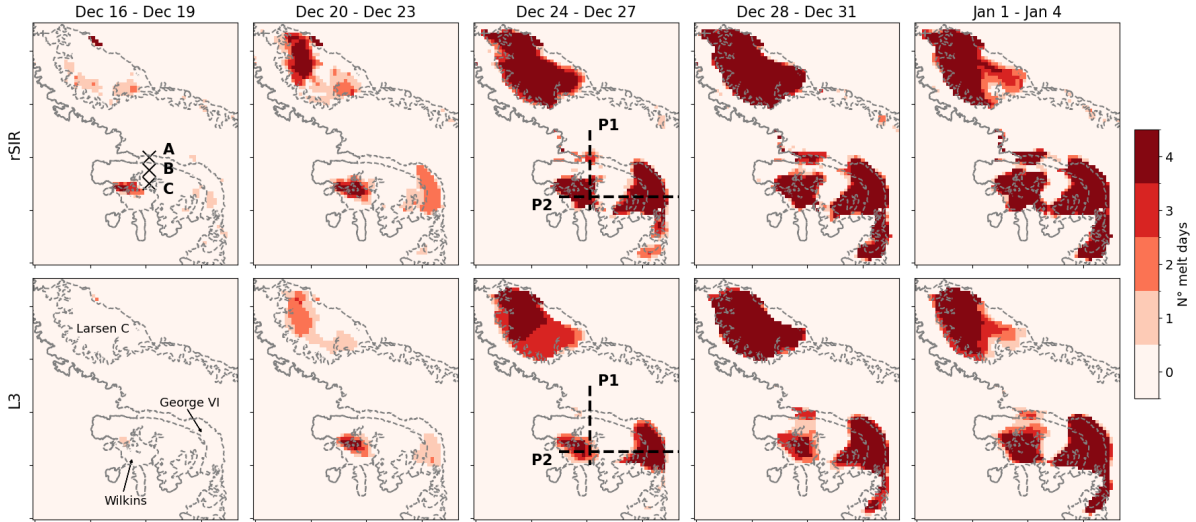


Figure 9: Illustration of the melt onset in the Antarctic Peninsula in 2018-2019. Each map shows the number of melt days over a 4 day period for rSIR (top row) and L3TB (bottom row). Pixels A, B and C correspond to the time series in Figure 11 and P1 and P2 represent the transects shown in Figure 10.

373 This localized larger melt signal in the lower resolution L3TB could be due to both the conservative 5 K threshold  
 374 on  $T_B^V$  used to define the dry snow mask on Greenland for the SiER<sub>40</sub> product, and to the mixing of dry and wet  
 375 snow regions in the L3TB, as noted in Antarctica around the grounding line. The effect of the conservative  
 376 5 K threshold adopted is noticeable elsewhere, for example in 2023 where the baseline product based on the  
 377 L3TB features many false alarms in the East and Northeast Greenland while these regions are filtered out in the  
 378 enhanced resolution product.

#### 379 4.3.2. Investigation of a melt event in the Antarctic Peninsula

380 To further investigate the reason of the larger number of melt days detected in the SiER<sub>40</sub> product, we focus  
 381 on a specific melt event. Figure 9 shows the number of melt days on the Antarctic Peninsula in five consecutive  
 382 4 day periods from December 16, 2018 to January 4, 2019. Going into the summer, melt propagates rapidly to  
 383 the entire Wilkins, George VI and Larsen C ice shelves. Melt is detected earlier and with a wider extent in the  
 384 SiER<sub>40</sub> product (top row) compared to the L3TB product (bottom row), especially in the northern George VI ice  
 385 shelf.

386 Figure 10 presents the difference between the average  $T_B^H$  on December 24-27<sup>th</sup>, 2018 and the average winter  
 387  $T_B^H$  ( $\Delta T_B^H$ ) along the transects P1 and P2. P1 crosses the Wilkins and northern George VI ice shelves, while P2  
 388 crosses the Wilkins, Bach and Southern George VI ice shelves (see Figure 9). We also show the melt detection  
 389 threshold along P1 and P2 for the L3TB and rSIR products to identify areas where  $\Delta T_B^H$  is larger, corresponding to  
 390 melting regions detected by the adaptive threshold algorithm. A large peak in  $\Delta T_B^H$  is associated to the crossing  
 391 of each ice shelf. This peak in summer  $T_B$  is also present but smoothed in the L3TB product. This results in  
 392 the SiER<sub>40</sub> product rising above the melt detection threshold more frequently than the L3TB. On the northern  
 393 George VI ice shelf (P1, right peak), the L3TB product does not reach the melt detection threshold while the  
 394 SiER<sub>40</sub> does. This mainly explains the large increase in annual melt days observed in the northern George VI ice

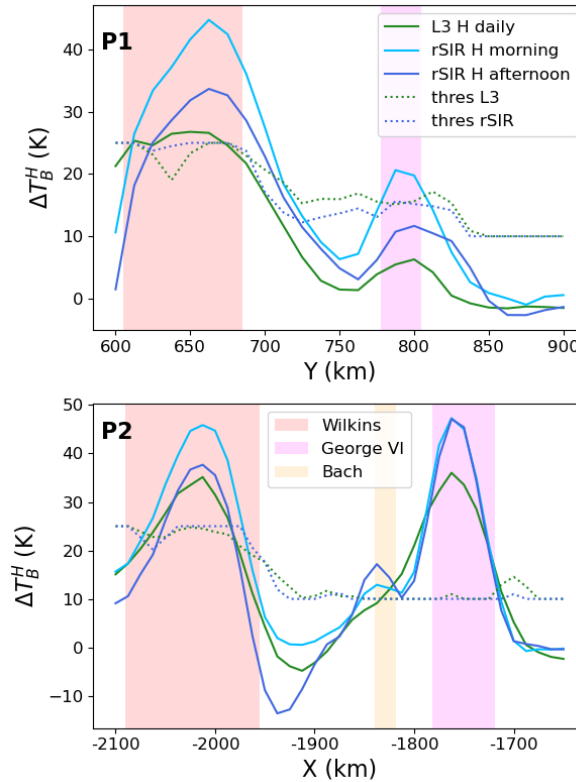


Figure 10: Difference ( $\Delta T_B^H$ ) between the average  $T_B^H$  on December 27-30th, 2018 and the average winter  $T_B^H$  computed from June 1st to August 31st, 2018, along two transects in Y (P1) and X (P2) crossing the George VI and Wilkins ice shelves. P1 and P2 are identified in Figure 9 which also shows the intensive melt occurring during the 4-day interval on both ice shelves.

395 shelf when using the new enhanced resolution dataset compared to the L3TB (see Figure 7).

396 To explain further the differences observed between the number of melt days detected by the two products,  
 397 Figure 11 presents the time series of  $T_B^H$  at the locations of pixels A, B and C shown in Figure 9. The melt days  
 398 detected by the L3TB product (green bars) and the SiER<sub>40</sub> (blue bars) are indicated at the bottom of each plot.  
 399 Pixel A is located on the northern George VI ice shelf. Here, the peak in  $T_B^H$  is smoothed in the L3TB compared  
 400 to the SiER<sub>40</sub>, and as a consequence the latter indicates more melt (67 days) than the former (48 days). Pixel  
 401 B is located on the mountain range separating the George VI and Wilkins ice shelves. Here, melt is less likely  
 402 due to higher altitude (mountain ranges >1500 m) and results mainly from the contamination of SMOS signal  
 403 by surrounding wet snow areas. The amplitude of  $T_B^H$  variations in the SiER<sub>40</sub> is lower than in the L3TB, which  
 404 results in a lower number of melt days (15 instead of 31). Finally, pixel C is located nearby the grounding line  
 405 of Wilkins ice shelf in a region with intense melt. Both products show a strong seasonal increase in  $T_B^H$  and the  
 406 number of melt days detected is slightly higher in the SiER<sub>40</sub> (68 days) than in the L3TB (60 days).

## 407 5. Discussion

408 We have used the SMOS L1C as the unique input of the well-established rSIR algorithm to reconstruct en-  
 409 hanced resolution  $T_B$  maps for SMOS, in order to assess the possible gain in spatial resolution and the impact on  
 410 melt detection. This process involved several methodological choices and adaptations of the baseline algorithms

411 that are discussed in this section.

### 412 5.1. Tradeoff between noise, coverage and spatial resolution

413 The application of the rSIR algorithm to SMOS involved several critical choices which were made for a tar-  
414 geted application, the melt detection. We discuss here these choices and their influence on the balance between  
415 noise level, spatial resolution and coverage, and how they could be adjusted for other applications.

416 A first tradeoff between the noise and the coverage is related to the choices of the poor data rejection criteria.  
417 The area within a SMOS snapshot with lowest noise is centered along-track at approximately 35-40° incidence  
418 angle, while the noisiest parts are located near nadir and close to the border of the track, as shown in Figure 2c.  
419 The selection of the best data only tends to reduce the width of SMOS tracks. Melt detection can accommodate  
420 a higher noise as it consists in detecting  $T_B$  variations of several tens of Kelvin, while the best possible coverage  
421 is required to follow its daily or sub-daily variations. The SiER<sub>40</sub> product was therefore computed accepting a  
422 high radiometric accuracy threshold of 5 K for a single measurement and it achieves a coverage of 99 % of the  
423 Antarctic pixels every day. As a consequence, the average radiometric accuracy is high (<2 K) in the center and  
424 lower (~4 K) near the border of the tracks. Other applications requiring higher accuracy should reject more data  
425 and deal with a reduced coverage or temporal revisit.

426 A second tradeoff is between noise and spatial resolution, and depends on two settings. Firstly, the low-  
427 incidence observations are likely noisier but also have the highest native spatial resolution which led us to select  
428 incidence bins at 40° and lower. Low-incidence measurements could be excluded for other applications to ensure  
429 a better radiometric accuracy. Secondly, the number of iterations in the image reconstruction process controls  
430 the enhancement and the noise of  $T_B$  maps. The rSIR algorithm was applied in previous studies to conventional  
431 radiometers with low noise (~1 K or lower, (Long & Brodzik, 2016; Long et al., 2019)). In principle, the use of  
432 noisier raw data from SMOS logically limits the achievable spatial resolution of the image reconstruction as  
433 the iterations must be stopped earlier. For this reason, a threshold of 10 iterations is adopted in this study  
434 for SMOS which is lower than the typical 20 iterations threshold of the NSIDC products for SSM/I, SSMIS,  
435 AMSR-E and SMAP (Long & Brodzik, 2016; Long et al., 2019). This may explain the slightly reduced effective

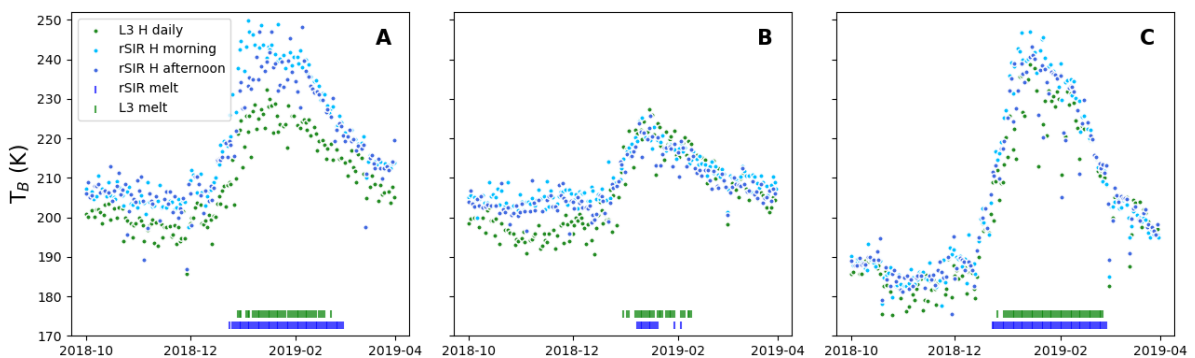


Figure 11: Time series of  $T_B^H$  for SMOS L3TB and SiER<sub>40</sub> products from April 2018 to March 2019 for the pixels marked at locations A, B and C in Figure 6 and Figure 7 on Antarctic ice shelves. The blue (green, respectively) bars at the bottom of each subplot indicate the days where melt is detected using the SiER<sub>40</sub> (L3TB).

436 spatial resolution of the SiER<sub>40</sub> compared with the SMAP rSIR-enhanced product (difference  $\leq 3$  km, Table 3).  
437 In practice, the selection of observations with a larger radiometric accuracy (e.g. located on the border of the  
438 tracks) does not seem to have a strong impact on the reconstruction of SMOS  $T_B$ , as we obtained an equivalent  
439 spatial resolution for the range of accuracy 2.8–5 K. We also found that a reconstruction with 15 iterations (not  
440 shown) provided no significant improvement in spatial resolution, but a higher noise. The potential of further  
441 resolution enhancement for SMOS using the rSIR algorithm is therefore likely limited.

## 442 5.2. Multi-incidence dataset

443 The use of multi-incidence measurements from  $\sim 15^\circ$  to  $40^\circ$  in the MiER product aimed to select data with the  
444 best native spatial resolution, but it requires to normalize the variations of  $T_B$  depending on the incidence angle  
445 using the MFTE model. It turns out that the physical model is unable to reproduce SMOS incidence diagrams,  
446 especially close to nadir. A similar issue was observed between SMOS incidence diagrams and the in-situ L-band  
447 radiometer RADOMEX installed at Dome C in 2010 (see figure 14 in Macelloni et al. (2013)). We suspect that  
448 the conversion of the measurements from the XY antenna frame to the HV surface frame used in geophysics  
449 could be responsible for this non-physical behavior. A direct use of XY brightness temperatures in geophysical  
450 applications is less common but could prevent this issue. In our approach, we used a more flexible semi-physical  
451 model to fit SMOS incidence diagrams as we are only interested in the normalization of all observations to a  
452 fixed incidence angle.

453 During the evaluation of the spatial resolution, we observed that the MiER and SiER<sub>40</sub> products have almost  
454 the same resolution (see Table 3). As our results suggest that the additional complexity and computing cost of the  
455 multi-incidence approach are not worth the result, we finally adopted the SiER<sub>40</sub> product to detect melt. We have  
456 three hypotheses to explain why the inclusion of low-incidence observations does not enhance the resolution.  
457 First, the gain in native spatial resolution from  $40^\circ$  to the lowest incidence is relatively small compared to the  
458 large improvement between  $55^\circ$  and  $40^\circ$  (Figure 2a). Secondly, SMOS observations near nadir have a small spatial  
459 coverage so the reconstructed brightness temperature maps are dominated by data near  $40^\circ$ , especially close to  
460 the border of the tracks. Thirdly, the lowest incidence data have a higher radiometric accuracy which could limit  
461 the capability of the rSIR algorithm to reconstruct accurate  $T_B$  images. Overall, for applications requiring the  
462 knowledge of complete SMOS incidence diagrams with an enhanced resolution, a practical solution would be  
463 to compute enhanced resolution  $T_B$  maps for each incidence bin in the L3TB product.

## 464 5.3. Limitations and improvements of melt detection

465 The algorithm proposed in Leduc-Leballeur et al. (2020) to detect melt from the L3TB product requires minor  
466 modifications to be applicable to the enhanced resolution product. The characteristics of this new product and  
467 the necessary technical adjustments may have an impact on the melt detection algorithm in three different  
468 ways.

469 First, we had to modify the mask introduced in Leduc-Leballeur et al. (2020) to filter out regions where snow  
470 is always dry. In Antarctica, it concerns all the pixels where the standard deviation on  $T_B^V$  is lower than 2.8 K.  
471 This approach works well in Antarctica, but in Greenland we had to increase the threshold to 5 K to deal with  
472 the larger  $T_B$  variability. The additional noise in Greenland may be due to an incorrect RFI filtering using L1C  
473 flags, as we noticed a bunch of observations with  $T_B$  as large as 400 K. These outliers were filtered out using  
474 a simple thresholding. All the measurements with a  $T_B$  higher than 280 K are considered as non-physical and  
475 potentially affected by RFI, which is a fair assumption on the ice sheets. However, some observations with a  $T_B$   
476 lower than 280 K could still be affected by RFI and introduce noise in the reconstructed maps.

477 Secondly, the new SiER<sub>40</sub> product is noisier than the L3TB at 52.5° (Section 5.1) which is susceptible to disturb  
478 the melt detection algorithm. Isolated false alarms may occur due to outliers but this effect is difficult to evaluate,  
479 as it is also counterbalanced by the increase of the  $3\sigma$  melt detection threshold due to higher noise. This higher  $3\sigma$   
480 threshold can also reduce detection early and late in the season with the enhanced resolution product. However,  
481 this effect seems negligible given the otherwise considerable larger number of melt days observed throughout  
482 Antarctica and Greenland in the SiER<sub>40</sub> compared to the L3TB (see Figure 6 and Figure 7), corresponding to a  
483 clear snow wetting with large  $T_B$  variations as shown in Figure 10 and Figure 11.

484 Lastly, we used data with an incidence angle of 37.5–42.5° while Leduc-Leballeur et al. (2020) used the 50–55°  
485 bin from the L3TB product.  $T_B^H$  and  $T_B^V$  are respectively higher and lower at low-incidence compared to Brewster  
486 angle ( $\sim 55^\circ$ ). Nonetheless, the principle of the melt detection algorithm is based on the large difference observed  
487 between winter and summer  $T_B$ , that is still largely valid at 40° incidence (Figure 11 gives evidence of it). It is  
488 therefore assumed that the radiometric differences between the 40° and 52.5° datasets have a negligible effect  
489 on melt detection compared to the stronger effect of the resolution enhancement.

490 To conclude, small adjustments were performed in the melt detection algorithm to cope with the differences  
491 in the SiER<sub>40</sub> and L3TB products. However, their impact is unnoticeable compared to the main effect of the  
492 resolution enhancement.

## 493 6. Conclusion

494 We applied the state-of-the-art rSIR image reconstruction algorithm to SMOS L1C data to produce en-  
495 hanced resolution SMOS  $T_B$  maps. Three products were computed and evaluated, using the 50–55° incidence  
496 bin only (SiER<sub>52.5</sub>), the 37.5–42.5° incidence bin only (SiER<sub>40</sub>), and the observations with an incidence lower than  
497 40° (MiER). The comparisons against the SMOS L3TB product show no systematic bias except for the MiER prod-  
498 uct that requires a modelisation of incidence diagrams. The spatial resolution of the SiER<sub>40</sub> and MiER products  
499 is estimated to around 30 km, which is a  $\sim 30\%$  improvement (near 50%, respectively) with respect to the L3TB  
500 product at 40° (52.5°).

501 We evaluated the impacts of this resolution enhancement for melt detection using the SiER<sub>40</sub> product against  
502 the L3TB at 52.5° previously used in Leduc-Leballeur et al. (2020). At global scale, there is a widespread in-

503 crease of the annual average number of melt days detected in both the Greenland and Antarctic ice sheets. The  
504 largest melt enhancements (>30 days/year) are found in Greenland's percolation areas and on many Antarctic  
505 ice shelves, especially near the grounding line. We demonstrated through a case study in the Antarctic Penin-  
506 sula that this gain is due to a lesser dilution of the signal produced by localized melt when the surrounding  
507 snow areas remain dry. As a consequence, an earlier and sharper increase in  $T_B$  is detected as melt in the SiER<sub>40</sub>  
508 product while snow status is still dry in the L3TB. The wet snow detected is also located more accurately on the  
509 ice shelves. A sharper  $T_B$  decrease in the SiER<sub>40</sub> than in the L3TB just above the grounding lines corresponds to  
510 the only pixels with more melt days in the L3TB product.

511 These findings and the datasets produced are important for future studies in large-scale hydrology of the ice  
512 sheets. First, they could feed L-band and multi-frequency algorithms that aim to detect aquifers, study melt-  
513 water percolation and melt/refreeze diurnal cycles. The spatial resolution achieved in the enhanced resolution  
514 product (~30 km) is comparable for instance to AMSR2 frequency-dependent footprints (~41 km at 6.9 GHz  
515 to ~8 km at 36.5 GHz), and SMOS time series extend to 2010. The enhanced resolution  $T_B$  maps are also a  
516 valuable input for future algorithms to estimate liquid water content. Finally, for purposes of designing the up-  
517 coming passive microwave satellite missions like ESA's Copernicus Imaging Microwave Radiometer (CIMR) and  
518 their retrieval algorithms, we demonstrated how important is the spatial resolution when coming to geophysical  
519 applications, especially in the cryosphere sciences.

## 520 **Acknowledgements**

521 This work has been funded by the Centre National d'Etudes Spatiales (CNES) grants TOSCA SMOS-TE and  
522 SMOS-HR and supported by European Space Agency's 4DGreenland project. The authors would like to thank  
523 Marion Leduc-Leballeur for her discussions and help with the melt detection algorithm.

## 524 **References**

- 525 Abdalati, W., & Steffen, K. (1995). Passive microwave-derived snow melt regions on the Greenland ice sheet.  
526 *Geophysical Research Letters*, 22, 787–790.
- 527 Al Bitar, A., Mialon, A., Kerr, Y. H., Cabot, F., Richaume, P., Jacquette, E., Quesney, A., Mahmoodi, A., Tarot, S.,  
528 Parrens, M. et al. (2017). The global SMOS Level 3 daily soil moisture and brightness temperature maps. *Earth*  
529 *System Science Data*, 9, 293–315. doi:10.5194/essd-9-293-2017.
- 530 Ashcraft, I. S., & Long, D. G. (2006). Comparison of methods for melt detection over Greenland using active  
531 and passive microwave measurements. *International Journal of Remote Sensing*, 27, 2469–2488. doi:doi=10.  
532 1080/01431160500534465.

533 Banwell, A. F., MacAyeal, D. R., & Sergienko, O. V. (2013). Breakup of the Larsen B Ice Shelf triggered by  
534 chain reaction drainage of supraglacial lakes. *Geophysical Research Letters*, *40*, 5872–5876. doi:10.1002/  
535 2013GL057694.

536 Banwell, A. F., Willis, I. C., Macdonald, G. J., Goodsell, B., & MacAyeal, D. R. (2019). Direct measurements of  
537 ice-shelf flexure caused by surface meltwater ponding and drainage. *Nature communications*, *10*, 730. doi:10.  
538 1038/s41467-019-08522-5.

539 Bell, R. E., Chu, W., Kingslake, J., Das, I., Tedesco, M., Tinto, K. J., Zappa, C. J., Frezzotti, M., Boghosian, A., &  
540 Lee, W. S. (2017). Antarctic ice shelf potentially stabilized by export of meltwater in surface river. *Nature*, *544*,  
541 344–348. doi:10.1038/nature22048.

542 Bevan, S. L., Luckman, A. J., Kuipers Munneke, P., Hubbard, B., Kulesa, B., & Ashmore, D. W. (2018). Decline  
543 in surface melt duration on Larsen C ice shelf revealed by the Advanced Scatterometer (ASCAT). *Earth and*  
544 *Space Science*, *5*, 578–591.

545 Brodzik, M. J., & Long, D. G. (2018). Calibrated Passive Microwave Daily EASE-Grid 2.0 Brightness Temper-  
546 ature ESDR (CETB): Algorithm Theoretical Basis Document. URL: [https://nsidc.org/sites/  
547 default/files/documents/technical-reference/measurements\\_cetb\\_atbd\\_v1.pdf](https://nsidc.org/sites/default/files/documents/technical-reference/measurements_cetb_atbd_v1.pdf)  
548 accessed: 7-12-2023.

549 Brodzik, M. J., Long, D. G., & Hardman, M. A. (2021). SMAP Radiometer Twice-Daily rSIR-enhanced EASE-Grid  
550 2.0 Brightness Temperatures, Version 2. doi:10.5067/YAMX52BXFL10.

551 Colliander, A., Mousavi, M., Kimball, J. S., Miller, J. Z., & Burgin, M. (2023). Spatial and temporal differences  
552 in surface and subsurface meltwater distribution over Greenland ice sheet using multi-frequency passive mi-  
553 crowave observations. *Remote Sensing of Environment*, *295*, 113705.

554 Colliander, A., Mousavi, M., Marshall, S., Samimi, S., Kimball, J. S., Miller, J. Z., Johnson, J., & Burgin, M. (2022).  
555 Ice Sheet Surface and Subsurface Melt Water Discrimination Using Multi-Frequency Microwave Radiometry.  
556 *Geophysical Research Letters*, *49*, e2021GL096599. doi:10.1029/2021GL096599.

557 Entekhabi, D., Njoku, E. G., O'Neill, P. E., Kellogg, K. H., Crow, W. T., Edelstein, W. N., Entin, J. K., Goodman,  
558 S. D., Jackson, T. J., Johnson, J. et al. (2010). The soil moisture active passive (SMAP) mission. *Proceedings of*  
559 *the IEEE*, *98*, 704–716. doi:10.1109/JPROC.2010.2043918.

560 ESA (2021). SMOS Level 1 and Auxiliary Data Products Specifications. URL: [https://earth.esa.int/  
561 eogateway/catalog/smos-science-products](https://earth.esa.int/eogateway/catalog/smos-science-products) accessed: 7-12-2023.

562 Fettweis, X., Box, J. E., Agosta, C., Amory, C., Kittel, C., Lang, C., van As, D., Machguth, H., & Gallée, H. (2017).  
563 Reconstructions of the 1900–2015 Greenland ice sheet surface mass balance using the regional climate MAR  
564 model. *The Cryosphere*, *11*, 1015–1033. doi:10.5194/tc-11-1015-2017.



565 Houtz, D., Mätzler, C., Naderpour, R., Schwank, M., & Steffen, K. (2021). Quantifying surface melt and liquid  
566 water on the Greenland ice sheet using L-band radiometry. *Remote Sensing of Environment*, 256, 112341.  
567 doi:10.1016/j.rse.2021.112341.

568 IMBIE (2018). Mass balance of the Antarctic Ice Sheet from 1992 to 2017. *Nature*, 558, 219–222.

569 IMBIE (2020). Mass balance of the Greenland Ice Sheet from 1992 to 2018. *Nature*, 579, 233–239.

570 Kerr, Y. H., Waldteufel, P., Wigneron, J.-P., Delwart, S., Cabot, F., Boutin, J., Escorihuela, M.-J., Font, J., Reul, N.,  
571 Gruhier, C., Juglea, S. E., Drinkwater, M. R., Hahne, A., Martín-Neira, M., & Mecklenburg, S. (2010). The smos  
572 mission: New tool for monitoring key elements of the global water cycle. *Proceedings of the IEEE*, 98, 666–687.  
573 doi:10.1109/JPROC.2010.2043032.

574 Kerr, Y. H., Waldteufel, P., Wigneron, J.-P., Martinuzzi, J., Font, J., & Berger, M. (2001). Soil moisture retrieval  
575 from space: The Soil Moisture and Ocean Salinity (SMOS) mission. *IEEE transactions on Geoscience and remote  
576 sensing*, 39, 1729–1735. doi:10.1109/36.942551.

577 Kingslake, J., Ely, J. C., Das, I., & Bell, R. E. (2017). Widespread movement of meltwater onto and across Antarctic  
578 ice shelves. *Nature*, 544, 349–352. doi:10.1038/nature22049.

579 Koenig, L. S., Miège, C., Forster, R. R., & Brucker, L. (2014). Initial in situ measurements of perennial meltwater  
580 storage in the Greenland firn aquifer. *Geophysical Research Letters*, 41, 81–85.

581 Kuipers Munneke, P., Luckman, A., Bevan, S., Smeets, C., Gilbert, E., Van Den Broeke, M., Wang, W., Zender,  
582 C., Hubbard, B., Ashmore, D. et al. (2018). Intense winter surface melt on an Antarctic ice shelf. *Geophysical  
583 Research Letters*, 45, 7615–7623. doi:https://doi.org/10.1029/2018GL077899.

584 Leduc-Leballeur, M., Picard, G., Macelloni, G., Mialon, A., & Kerr, Y. H. (2020). Melt in Antarctica derived from  
585 Soil Moisture and Ocean Salinity (SMOS) observations at L band. *The Cryosphere*, 14, 539–548. doi:10.  
586 5194/tc-14-539-2020.

587 Liang, D., Guo, H., Zhang, L., Cheng, Y., Zhu, Q., & Liu, X. (2021). Time-series snowmelt detection over the  
588 Antarctic using Sentinel-1 SAR images on Google Earth Engine. *Remote Sensing of Environment*, 256, 112318.  
589 doi:10.1016/j.rse.2021.112318.

590 Liu, H., Wang, L., & Jezek, K. C. (2006). Spatiotemporal variations of snowmelt in Antarctica derived from satellite  
591 scanning multichannel microwave radiometer and Special Sensor Microwave Imager data (1978–2004). *Journal  
592 of Geophysical Research: Earth Surface*, 111. doi:10.1029/2005JF000318.

593 Long, D. G. (2015). An Investigation of Antenna Patterns for the CETB. URL: [https://zenodo.org/  
594 records/7959217](https://zenodo.org/records/7959217) accessed: 7-12-2023.

595 Long, D. G., & Brodzik, M. J. (2016). Optimum Image Formation for Spaceborne Microwave Radiometer Prod-  
596 ucts. *IEEE Transactions on Geoscience and Remote Sensing*, *54*, 2763–2779. doi:10.1109/TGRS.2015.  
597 2505677.

598 Long, D. G., Brodzik, M. J., & Hardman, M. A. (2019). Enhanced-Resolution SMAP Brightness Temperature  
599 Image Products. *IEEE Transactions on Geoscience and Remote Sensing*, *57*, 4151–4163. doi:10.1109/TGRS.  
600 2018.2889427.

601 Long, D. G., & Daum, D. L. (1998). Spatial resolution enhancement of SSM/I data. *IEEE Transactions on Geoscience  
602 and Remote Sensing*, *36*, 407–417.

603 Luckman, A., Elvidge, A., Jansen, D., Kulesa, B., Munneke, P. K., King, J., & Barrand, N. E. (2014). Surface melt  
604 and ponding on Larsen C Ice Shelf and the impact of föhn winds. *Antarctic Science*, *26*, 625–635.

605 Macelloni, G., Brogioni, M., Pettinato, S., Zasso, R., Crepez, A., Zaccaria, J., Padovan, B., & Drinkwater, M.  
606 (2013). Ground-based L-band emission measurements at Dome-C Antarctica: The DOMEX-2 experiment.  
607 *IEEE transactions on geoscience and remote sensing*, *51*, 4718–4730.

608 Macelloni, G., Leduc-Leballeur, M., Montomoli, F., Brogioni, M., Ritz, C., & Picard, G. (2019). On the retrieval  
609 of internal temperature of Antarctica ice sheet by using SMOS observations. *Remote Sensing of Environment*,  
610 *233*, 111405. doi:10.1016/j.rse.2019.111405.

611 Maezawa, H., & Miyauchi, H. (2009). Rigorous expressions for the Fresnel equations at interfaces between  
612 absorbing media. *JOSA A*, *26*, 330–336. doi:10.1364/JOSAA.26.000330.

613 Miège, C., Forster, R. R., Brucker, L., Koenig, L. S., Solomon, D. K., Paden, J. D., Box, J. E., Burgess, E. W., Miller,  
614 J. Z., McNerney, L. et al. (2016). Spatial extent and temporal variability of Greenland firn aquifers detected by  
615 ground and airborne radars. *Journal of Geophysical Research: Earth Surface*, *121*, 2381–2398.

616 Miller, J. Z., Culberg, R., Long, D. G., Shuman, C. A., Schroeder, D. M., & Brodzik, M. J. (2022). An empirical  
617 algorithm to map perennial firn aquifers and ice slabs within the Greenland Ice Sheet using satellite L-band  
618 microwave radiometry. *The Cryosphere*, *16*, 103–125.

619 Miller, O., Solomon, D. K., Miège, C., Koenig, L., Forster, R., Schmerr, N., Ligtenberg, S. R., Legchenko, A., Voss,  
620 C. I., Montgomery, L. et al. (2020). Hydrology of a perennial firn aquifer in Southeast Greenland: an overview  
621 driven by field data. *Water Resources Research*, *56*, e2019WR026348.

622 Mote, T. L. (2007). Greenland surface melt trends 1973–2007: Evidence of a large increase in 2007. *Geophysical  
623 Research Letters*, *34*.

624 Mougnot, J., Rignot, E., Bjørk, A. A., Van den Broeke, M., Millan, R., Morlighem, M., Noël, B., Scheuchl, B., &  
625 Wood, M. (2019). Forty-six years of Greenland ice sheet mass balance from 1972 to 2018. *Proceedings of the  
626 national academy of sciences*, *116*, 9239–9244. doi:10.1073/pnas.1904242116.

627 Mousavi, M., Colliander, A., Miller, J. Z., & Kimball, J. S. (2022). A Novel Approach to Map the Intensity of  
628 Surface Melting on the Antarctica Ice Sheet Using SMAP L-Band Microwave Radiometry. *IEEE Journal of*  
629 *Selected Topics in Applied Earth Observations and Remote Sensing*, 15, 1724–1743. doi:10.1109/JSTARS.  
630 2022.3147430.

631 Nghiem, S., Hall, D., Mote, T., Tedesco, M., Albert, M., Keegan, K., Shuman, C., DiGirolamo, N., & Neumann, G.  
632 (2012). The extreme melt across the Greenland ice sheet in 2012. *Geophysical Research Letters*, 39.

633 Otosaka, I. N., Horwath, M., Mottram, R., & Nowicki, S. (2023). Mass balances of the Antarctic and Greenland ice  
634 sheets monitored from space. *Surveys in Geophysics*, (pp. 1–38). doi:10.5194/essd-15-1597-2023.

635 Picard, G., & Fily, M. (2006). Surface melting observations in Antarctica by microwave radiometers: Correcting  
636 26-year time series from changes in acquisition hours. *Remote Sensing of Environment*, 104, 325–336. doi:10.  
637 1016/j.rse.2006.05.010.

638 Picard, G., Fily, M., & Gallée, H. (2007). Surface melting derived from microwave radiometers: a climatic indicator  
639 in Antarctica. *Annals of Glaciology*, 46, 29–34. doi:10.3189/172756407782871684.

640 Picard, G., Leduc-Leballeur, M., Banwell, A. F., Brucker, L., & Macelloni, G. (2022). The sensitivity of satellite  
641 microwave observations to liquid water in the antarctic snowpack. *The Cryosphere*, 16, 5061–5083. doi:10.  
642 5194/tc-16-5061-2022.

643 Piepmeier, J. R., Focardi, P., Horgan, K. A., Knuble, J., Ehsan, N., Lucey, J., Brambora, C., Brown, P. R., Hoffman,  
644 P. J., French, R. T., Mikhaylov, R. L., Kwack, E.-Y., Slimko, E. M., Dawson, D. E., Hudson, D., Peng, J., Mo-  
645 hammed, P. N., De Amici, G., Freedman, A. P., Medeiros, J., Sacks, F., Estep, R., Spencer, M. W., Chen, C. W.,  
646 Wheeler, K. B., Edelstein, W. N., O'Neill, P. E., & Njoku, E. G. (2017). SMAP L-Band Microwave Radiometer: In-  
647 strument Design and First Year on Orbit. *IEEE Transactions on Geoscience and Remote Sensing*, 55, 1954–1966.  
648 doi:10.1109/TGRS.2016.2631978.

649 Ramage, J. M., & Isacks, B. L. (2002). Determination of melt-onset and refreeze timing on southeast Alaskan  
650 icefields using SSM/I diurnal amplitude variations. *Annals of Glaciology*, 34, 391–398.

651 Rignot, E., Mouginot, J., Scheuchl, B., Van Den Broeke, M., Van Wessem, M. J., & Morlighem, M. (2019). Four  
652 decades of Antarctic ice sheet mass balance from 1979–2017. *Proceedings of the National Academy of Sciences*,  
653 116, 1095–1103. doi:10.1073/pnas.1812883116.

654 Rott, H., Rack, W., Skvarca, P., & De Angelis, H. (2002). Northern Larsen ice shelf, Antarctica: Further retreat  
655 after collapse. *Annals of glaciology*, 34, 277–282.

656 Rott, H., Skvarca, P., & Nagler, T. (1996). Rapid collapse of northern Larsen ice shelf, Antarctica. *Science*, 271,  
657 788–792.

658 Sahr, K., White, D., & Kimerling, A. J. (2003). Geodesic discrete global grid systems. *Cartography and Geographic*  
659 *Information Science*, 30, 121–134.

660 Saunderson, D., Mackintosh, A., McCormack, F., Jones, R. S., & Picard, G. (2022). Surface melt on the Shackleton  
661 Ice Shelf, East Antarctica (2003–2021). *The Cryosphere*, 16, 4553–4569.

662 Scambos, T., Fricker, H. A., Liu, C.-C., Bohlander, J., Fastook, J., Sargent, A., Massom, R., & Wu, A.-M. (2009). Ice  
663 shelf disintegration by plate bending and hydro-fracture: Satellite observations and model results of the 2008  
664 Wilkins ice shelf break-ups. *Earth and Planetary Science Letters*, 280, 51–60.

665 Scambos, T. A., Bohlander, J., Shuman, C. A., & Skvarca, P. (2004). Glacier acceleration and thinning after  
666 ice shelf collapse in the Larsen B embayment, Antarctica. *Geophysical Research Letters*, 31. doi:10.1029/  
667 2004GL020670.

668 Scambos, T. A., Hulbe, C., Fahnestock, M., & Bohlander, J. (2000). The link between climate warming and  
669 break-up of ice shelves in the Antarctic Peninsula. *Journal of Glaciology*, 46, 516–530. doi:10.3189/  
670 172756500781833043.

671 Stokes, C. R., Sanderson, J. E., Miles, B. W., Jamieson, S. S., & Leeson, A. A. (2019). Widespread distribution of  
672 supraglacial lakes around the margin of the East Antarctic Ice Sheet. *Scientific reports*, 9, 13823.

673 Tedesco, M. (2007). Snowmelt detection over the Greenland ice sheet from SSM/I brightness temperature daily  
674 variations. *Geophysical Research Letters*, 34. doi:10.1029/2006GL028466.

675 Tedesco, M., & Fettweis, X. (2020). Unprecedented atmospheric conditions (1948–2019) drive the 2019 ex-  
676 ceptional melting season over the Greenland ice sheet. *The Cryosphere*, 14, 1209–1223. doi:10.5194/  
677 tc-14-1209-2020.

678 Torinesi, O., Fily, M., & Genthon, C. (2003). Variability and trends of the summer melt period of Antarctic ice  
679 margins since 1980 from microwave sensors. *Journal of Climate*, 16, 1047–1060.

680 Trusel, L., Frey, K. E., & Das, S. B. (2012). Antarctic surface melting dynamics: Enhanced perspectives from radar  
681 scatterometer data. *Journal of Geophysical Research: Earth Surface*, 117.

682 Wille, J. D., Favier, V., Dufour, A., Gorodetskaya, I. V., Turner, J., Agosta, C., & Codron, F. (2019). West  
683 antarctic surface melt triggered by atmospheric rivers. *Nature Geoscience*, 12, 911–916. doi:10.1038/  
684 s41561-019-0460-1.

685 Williamson, A. G., Banwell, A. F., Willis, I. C., & Arnold, N. S. (2018). Dual-satellite (Sentinel-2 and Land-  
686 sat 8) remote sensing of supraglacial lakes in Greenland. *The Cryosphere*, 12, 3045–3065. doi:10.5194/  
687 tc-12-3045-2018.

- 688 Wu, L., Torres, F., Corbella, I., Duffo, N., Durán, I., Vall-Ilossera, M., Camps, A., Delwart, S., & Martín-Neira,  
689 M. (2013). Radiometric performance of smos full polarimetric imaging. *IEEE Geoscience and Remote Sensing*  
690 *Letters*, *10*, 1454–1458. doi:10.1109/LGRS.2013.2260128.
- 691 Yang, K., & Smith, L. C. (2013). Supraglacial Streams on the Greenland Ice Sheet Delineated From Combined  
692 Spectral–Shape Information in High-Resolution Satellite Imagery. *IEEE Geoscience and Remote Sensing Letters*,  
693 *10*, 801–805. doi:10.1109/LGRS.2012.2224316.
- 694 Zwally, H. J. (1977). Microwave emissivity and accumulation rate of polar firn. *Journal of Glaciology*, *18*, 195–215.
- 695 Zwally, H. J., & Fiegles, S. (1994). Extent and duration of Antarctic surface melting. *Journal of Glaciology*, *40*,  
696 463–475.

697 **Appendix A. Description of the Multi-Fresnel Thermal Emission model**

698 The model applies to a slab of  $n$  horizontal layers  $i = 1 \dots n$  with given optical depth  $\tau_i$ , relative permittivity  
 699  $\epsilon_i$  and temperature  $T_i$ . The model neglects scattering so that the optical depth can be calculated as the product  
 700 of the layer thickness  $d_i$  and absorption coefficient  $\kappa_{ai}$ .

701 Let  $J_i^{t,b}$  and  $I_i^{t,b}$  be the upwelling and downwelling radiation at the top ( $t$  superscript) and bottom ( $b$  super-  
 702 script) of layer  $i$  propagating with a zenith angle  $\theta_i$ . The goal is to calculate the upwelling radiation emerging  
 703 at the surface of the slab, in the atmosphere (formally denoted by the index  $i = 0$ ):  $J_0^b$ . For this we formulate 1)  
 704 the angles of propagation in the layers, 2) the propagation through layers, 2) the transfer through the interfaces  
 705 between the layers and 3) the enforcement of the boundary conditions at the top and bottom of the slab.

706 *Zenith angle of propagation*

707 Applying the Snell-Descartes formula for loosely media (Maetzawa & Miyauchi, 2009) to account for the re-  
 708 fraction between the layers relates the propagation angle  $\theta_i$  in every layer  $i$  to the angle in the air  $\theta_0$ :

$$\mu_i = \frac{\Re \sqrt{\epsilon_i - \epsilon_0(1 - \mu_0^2)}}{\Re \sqrt{\epsilon_i}} \quad (\text{A.1})$$

709 where we have defined the cosine  $\mu_i = \cos(\theta_i)$ , and  $\Re$  denotes the real part.  $\mu_i$  is guaranteed to be  $\leq 1$  because  
 710 the air is the less refractive material.

711 *Propagation within the layers*

712 The downwelling radiation at the bottom of layer  $i$  is the result of the downwelling radiation coming from  
 713 the top of the layer and reaching the bottom with an attenuation equals to  $A_k = \exp(-\tau_i/\mu)$ , and by the natural  
 714 thermal emission within the layer which is the product of the emissivity and temperature  $T_i$ . The emissivity is  
 715 equal to the opacity of the layer, i.e.  $(1 - \exp(-\tau_k/\mu))$  according to Kirchoff's law. Similarly for the upwelling  
 716 radiation at the top, the propagation through the layer including the emission forms a system of two equations:

$$I_i^b = \exp(-\tau_i/\mu)I_i^t + (1 - \exp(-\tau_i/\mu))T_i \quad (\text{A.2})$$

$$J_i^t = \exp(-\tau_i/\mu)J_i^b + (1 - \exp(-\tau_i/\mu))T_i \quad (\text{A.3})$$

717 which can be written in a matrix form as follows:

$$\begin{pmatrix} I_i^t \\ J_i^t \\ 1 \end{pmatrix} = \begin{pmatrix} 1/A_i & 0 & -(1/A_i - 1)T_i \\ 0 & A_i & (1 - A_i)T_i \\ 0 & 0 & 1 \end{pmatrix} \begin{pmatrix} I_i^b \\ J_i^b \\ 1 \end{pmatrix} \quad (\text{A.4})$$

718 with the radiation at the top of the layer on the left and the bottom on the right.

719 *Propagation through the interfaces*

720 For each interface, the upwelling and the downwelling radiation can be written as the sum of the reflected  
721 and the transmitted radiation, leading to the two following equations:

$$J_{i-1}^b = r_i I_{i-1}^b + t'_i J_i^t \quad (\text{A.5})$$

$$I_i^t = t_i I_{i-1}^b + r'_k J_i^t \quad (\text{A.6})$$

722 where  $r_i$  and  $t_i$  are the reflection and transmission coefficient from layer  $i - 1$  to layer  $i$ , and  $r'_i$  and  $t'_i$  from  
723 layer  $i$  to layer  $i - 1$ . Given that the propagation angles in adjacent layers are related through Snell-Descarte's  
724 law,  $r'_i = r_i$  and  $t'_i = t_i$ , and by energy conservation  $t_i = 1 - r_i$ . Written in matrix form this yields:

$$\begin{pmatrix} I_{i-1}^b \\ J_{i-1}^b \\ 1 \end{pmatrix} = \frac{1}{1 - r_i} \begin{pmatrix} 1 & -r_i & 0 \\ r_i & 1 - 2r_i & 0 \\ 0 & 0 & 1 - r_k \end{pmatrix} \begin{pmatrix} I_k^t \\ J_k^t \\ 1 \end{pmatrix} \quad (\text{A.7})$$

725 *Combined transfer matrix*

726 Combining Equations A.4 and A.7 provides the transfer matrix  $M_i$  which links the radiance at the bottom of  
727 two successive layers:

$$M_i = \frac{1}{1 - r_1} \begin{pmatrix} P_i & -r_i P_i & (-(1/P_i - 1) - r_i(1 - P_i)) T_i \\ r_i/P_i & (1 - 2r_i) P_i & (-r_i(1/P_i - 1) + (1 - 2r_i)(1 - P_i)) T_i \\ 0 & 0 & 1 - r_i \end{pmatrix}. \quad (\text{A.8})$$

728 To represent the substrate at the bottom of the slab (characterized by its reflection coefficient  $r_{\text{sub}}$  and tem-  
729 perature  $T_{\text{sub}}$ ), it is possible to add a semi-infinite layer with the transfer matrix  $M_{n+1}$  given by Eq A.8 where  
730  $r_{n+1} = r_{\text{sub}}$  and  $T = T_{\text{sub}}$  and  $P_{n+1} = 0$ .

731 Then, combining the transfer matrices for each layer and the substrate leads to:

$$\begin{pmatrix} I_0^b = 0 \\ J_0^b \\ 1 \end{pmatrix} = \prod_{i=1}^{n+1} M_i \begin{pmatrix} I_n^b \\ J_n^b = 0 \\ 1 \end{pmatrix} \quad (\text{A.9})$$

732 where the downwelling radiation coming from the atmosphere at the top of the slab is  $I_0^b = 0$  and the upwelling  
733 radiation coming from the bottom of the infinite layer representing the substrate is  $J_{n+1}^b = 0$ .

734 *Emerging radiation*

735 Equation A.9 provides two linear equations with two unknowns  $J_0^b$  and  $I_n^b$ , which is solved to yield the  
736 emerging radiation at the top of the slab as follows:

$$J_0^b = (-m_{21}m_{13}/m_{11} + m_{23})/m_{33} \quad (\text{A.10})$$

737 where  $m_{jk}$  are the elements of the matrix  $\prod_{i=1}^{n+1} M_i$ . This solves the problem.